Two-dimensional Analysis of Conical Pulsed Inductive Plasma Thruster Performance

IEPC-2011-145

Presented at the 32nd International Electric Propulsion Conference, Wiesbaden, Germany
September 11-15, 2011

A. K. Hallock*
Princeton University, Princeton, NJ, 08544

K. A. Polzin†
NASA-Marshall Space Flight Center, Huntsville, AL 35812

G. D. Emsellem‡
The Elwing Company, Wilmington, DE, 19801

A model of the maximum achievable exhaust velocity of a conical theta pinch pulsed inductive thruster is presented. A semi-empirical formula relating coil inductance to both axial and radial current sheet location is developed and incorporated into a circuit model coupled to a momentum equation to evaluate the effect of coil geometry on the axial directed kinetic energy of the exhaust. Inductance measurements as a function of the axial and radial displacement of simulated current sheets from four coils of different geometries are fit to a two-dimensional expression to allow the calculation of the Lorentz force at any relevant averaged current sheet location. This relation for two-dimensional inductance, along with an estimate of the maximum possible change in gas-dynamic pressure as the current sheet accelerates into downstream propellant, enables the expansion of a one-dimensional circuit model to two dimensions. The results of this two-dimensional model indicate that radial current sheet motion acts to rapidly decouple the current sheet from the driving coil, leading to losses in axial kinetic energy 10-50 times larger than estimations of the maximum available energy in the compressed propellant. The decreased available energy in the compressed propellant as compared to that of other inductive plasma propulsion concepts suggests that a recovery in the directed axial kinetic energy of the exhaust is unlikely, and that radial compression of the current sheet leads to a loss in exhaust velocity for the operating conditions considered here.

Nomenclature

C	capacitance (F)	R_p, R_e	plasma, external resistance (Ω)
E	energy (J)	R_{coil}, R_{cs}	coil, current sheet major radius (m)
F_P	force (N)	r_{coil}, r_{cs}	coil, current sheet minor radius (m)
I_1, I_2	coil, plasma current (A)	$r, \bar{r}$	radial, average radial location (m)
k	Boltzmann's constant ($m^2kgs^{-2}K^{-1}$)	$\overline{r_{coil}}$	average coil radius (m)
L_0, L_C	parasitic, accessible inductance (H)	T_1	upstream temperature (K)
L_{tot}	total inductance (H)	u	shock velocity (m/s)
l_{coil}	coil length (m)	V, V_0	voltage, initial capacitor voltage (V)
M	mutual inductance (H)	$\mathbb{V}$	volume (m^3)
$\mathcal{M}$	Mach number	z	axial location (m)

*Graduate Research Assistant, Mechanical and Aerospace Engineering Department. ahallock@princeton.edu
†Propulsion Research Engineer, Propulsion Research and Technology Applications Branch, Propulsion Systems Department. kurt.a.polzin@nasa.gov
‡Chief Scientist, R & D Department, 1220 North Market Street, Suite 804. gregory.emsellem@elwingcorp.com

m_i, m_{bit}	ion mass, slug mass (kg)	z_0	axial decoupling distance (m)
$m(z)$	accelerated mass (kg)	α	half cone angle (degrees)
P_1, P_2	upstream, downstream pressure (Pa)	γ	specific heat ratio

I. Introduction

It is desirable to extend the lifetime and increase the reliability of an in-space propulsion system as much as possible since maintenance or replacement of that system becomes particularly challenging once it has been placed into orbit. Reducing the size and mass of the propulsion system, including the propellant required to complete a mission can permit an increase in the amount of payload as a percentage of total vehicle mass. The high values of specific impulse associated with electric propulsion (EP) reduces the amount of propellant needed for a given mission relative to other conventional propulsion systems.

Pulsed inductive plasma thrusters[1–3] are spacecraft propulsion devices in which electrical energy is capacitively stored and then discharged through an inductive coil. The thruster is electrodeless, with a time-varying current in the coil interacting with a plasma covering the face of the coil to induce a plasma current. Propellant is accelerated and expelled at a high exhaust velocity ($\mathcal{O}(10 - 100$ km/s)) by the Lorentz body force arising from the interaction of the magnetic field and the induced plasma current.

Thrusters of this type possess many demonstrated and potential benefits that make them worthy of continued investigation. The electrodeless nature of these thrusters eliminates the lifetime and contamination issues associated with electrode erosion in conventional electric thrusters. Also, a wider variety of propellants are available for use when compatibility with metallic electrodes in no longer an issue. Pulsed inductive accelerators have been successfully operated using propellants like ammonia, hydrazine, and CO_2, and there is no fundamental reason why they would not operate on other propellants like H_2O. It is well-known that pulsed accelerators can maintain constant specific impulse I_{sp} and thrust efficiency over a wide range of input power levels by adjusting the pulse rate to maintain a constant discharge energy per unit pulse. It has also been demonstrated that a pulsed inductive thruster operating in or near the regime of optimum dynamic impedance matching can operate at a relatively constant thrust efficiency over a wide range of I_{sp} values. Thrusters in this class have operated at high energy per pulse, and by increasing the pulse rate they offer the potential to process very high levels of power using a single thruster.

It has been found [1,2,4] that propellant utilization inefficiency can be a disadvantage for pulsed inductive thrusters with a flat inductive coil geometry. One proposed solution is the use of a nozzle downstream of the accelerating coil that injects propellant upstream onto the face of the inductive coil. This solution, however, presents the additional disadvantage of a physical body in the exhaust path of the propellant, adversely altering the propellant trajectory as the exhaust impacts (and erodes) the propellant injection structure.

A possible alternative solution to this problem is to alter the inductive coil geometry to better confine the neutral propellant within the region of interest where the processes of current sheet formation and acceleration occur. One alternative to a flat coil is a conic section or conical frustum. A flat, disc-shaped inductive coil can be considered as a conical inductive coil with a half cone angle of 90°, and as the half cone angle is decreased the fraction of axial electromagnetic force on the plasma current sheet decreases as the radial electromagnetic (pinching) force is increased. It is the purpose of this study to evaluate how interaction of the coil with the plasma current sheet and the propellant contained within is affected when a conical inductive coil geometry is employed. It should be noted that the effect of coil geometry on propellant utilization efficiency lies outside the scope of this work.

The rest of this paper describes the development of a semi-empirical expression for the loaded coil inductance as a function of the current sheet position in two dimensions, the incorporation of this new function into a well-known circuit model [2] for pulsed inductive thrusters, and a discussion of results for the parameter space of conical theta pinch pulsed inductive thrusters with an estimate of the axial kinetic energy losses incurred by pinching the propellant and the possible recovery of a portion of these losses through gas-dynamic effects.

II. One-Dimensional Inductive Accelerator Modeling

Pulsed inductive thrusters are commonly studied with the use of a semi-empirical circuit model coupled to a one dimensional momentum equation [2]. This circuit is shown in Fig. II, where I_1 is the current

flowing in the driving circuit, I_2 is the current flowing in the plasma current sheet, C is the capacitance of the capacitor, M is the mutual inductance between the driving coil and the current sheet, L_0 is the initial (parasitic) inductance, L_C is the accessible coil inductance, R_p is the resistance of the plasma, and R_e is the resistance in the driving circuit.

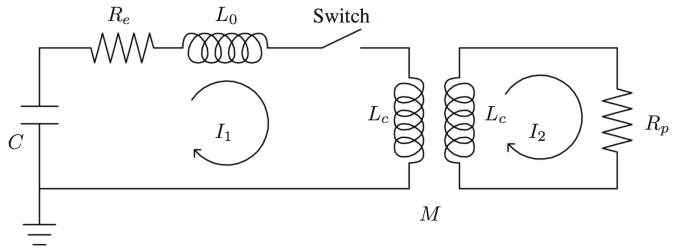

Figure 1. Lumped element circuit model of a pulsed inductive thruster inductively coupled to a plasma (taken from Ref. [2]).

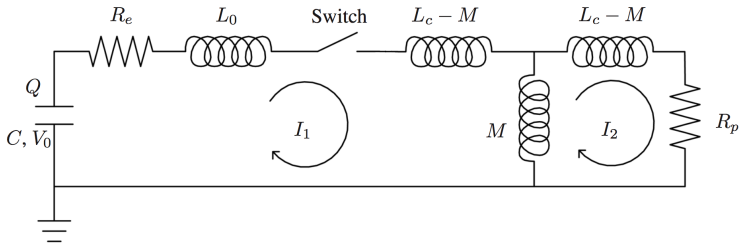

Figure 2. Equivalent circuit of a pulsed inductive thruster inductively coupled to a plasma used to derive a set of governing equations to model thruster performance.

The equivalent circuit, shown in Fig. 2, can be drawn and a set of equations can be derived to model thruster performance in terms of the electrical parameters. For this circuit, where V_0 is the initial voltage on the capacitor and V is the voltage on the capacitor as a function of time, the following equations follow from the application of Kirchoff's law:

$$\frac{dI_1}{dt} = \frac{L_C V - L_C R_e I_1 - M R_p I_2 + (L_C I_2 + M I_1)\frac{dM}{dt}}{L_C (L_0 + L_C) - M^2} \tag{1}$$

$$\frac{dI_2}{dt} = \frac{M\frac{dI_1}{dt} + I_1\frac{dM}{dt} - R_p I_2}{L_C} \tag{2}$$

$$\frac{dV}{dt} = \frac{-I_1}{C} \tag{3}$$

The equation of motion for the current sheet can be written using Newton's second law with the force acting on the current sheet arising from the magnetic pressure between the driving coil and the current sheet propellant mass in the sheet accumulating according to the snowplow model.

$$\frac{dv_z}{dt} = \left[\frac{L_C I_1^2}{2z_0}\exp\left(-\frac{z}{z_0}\right) - \rho_A(z)\, v_z^2\right] / m(z) \tag{4}$$

where z is the axial displacement of the current sheet from the driving coil, $m(z)$ is the total propellant mass in the current sheet, $\rho_A(z)$ is the linear mass density distribution, and v_z is the axial current sheet velocity.

$$\frac{dz}{dt} = v_z \tag{5}$$

For this study, the current sheet was modeled as a slug mass where all the propellant is assumed to be initially contained in the current sheet ($\rho_A(z) = 0$, $m_0 = m_{bit}$).

Adding the lumped inductive elements shown in Fig. 2 gives the total inductance,

$$L_{tot} = L_0 + L_C - \frac{M^2}{L_C}. \tag{6}$$

It can be seen from this equation that the total inductance changes as a function of time due to the time changing mutual inductance, which varies due to the movement of the current sheet. An expression for the mutual inductance as a function of current sheet axial position has been empirically determined [2] for a half-cone angle of 90° (i.e. flat coil) and has been found to accurately represent the axial inductive coupling behavior of ring-shaped and conical geometries as well [5, 6]:

$$L_{tot}(z) = L_0 + L_C \left(1 - \exp\left(-z/z_0\right)\right) \tag{7}$$

where z_0 is the decoupling distance. This expression is set equal to the previous expression for total inductance (Eq. 6) and solved for the mutual inductance as a function of the axial separation distance between the driving coil and the current sheet:

$$M = L_C \exp\left(-z/2z_0\right), \tag{8}$$

of which the time derivative is,

$$\frac{dM}{dt} = -\frac{L_C}{2z_0} \exp\left(-z/2z_0\right) \frac{dz}{dt}, \tag{9}$$

closing the set of six first-order ODEs, consisting of Eqs. 1, 2, 3, 4, 5, and 9, that can be readily solved numerically. Of these six governing equations only Eq. 9 must be empirically found based on the inductive coil geometry.

III. Experiment

Experiments were performed [7] to determine the inductive coupling of conical inductive coils of various geometries. The total inductance of each coil was measured as a function of the axial displacement of a copper frustum that simulates the presence of a current sheet with the assumption that the current sheet geometry will mirror the coil geometry that formed it. Two simulated current sheets were constructed for each coil, one fitting tightly against the inner surface of the coil and the second having a different minor radius r and major radius R to simulate radial compression (or pinching) of the current sheet. A diagram of coil and current sheet geometry is shown in Fig. 3. Pinching motion is assumed to leave the half cone angle α and coil length l_{coil} unchanged where l_{coil} is defined as:

$$l_{coil} = (R_{coil} - r_{coil})/\tan(\alpha).$$

The details of the construction process can be found in Ref. [7], and we only repeat the results of the experiment here. The coil geometries studied are listed in Table 1 and the current sheet geometries studied are listed in Table 2.

A. A Two-dimensional Empirical Expression for Inductance

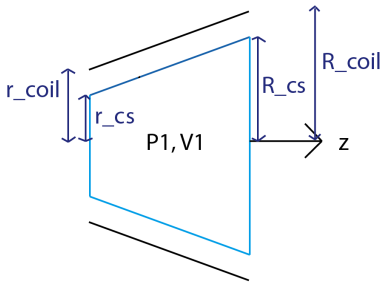

Figure 3. Geometry of the radial inductance model.

reference	α (degrees)	l_{coil} (cm)	r_{coil} (cm)
12	12	4.3	4
20S	20	5	4
20L	20	10	4
38	38	10	4

Table 1. Inductive coil geometries studied.

reference	α (degrees)	l_{coil} (cm)	r_{cs} (cm)
CS12	12	4.3	3.9
CS12P	12	4.3	2.5
CS20S	20	5	3.9
CS20SP	20	5	2.5
CS20L	20	10	3.9
CS20LP	20	10	2.5
CS38	38	10	3.9
CS38P	38	10	2.5

Table 2. Current sheet geometries studied.

The total inductance (L_{tot}) was measured at 84 locations using an Agilent 4285A precision LCR meter and is shown in Fig. 4 as a function of axial copper frustum displacement. Values of L_0, L_C, and z_0 were calculated for each coil geometry by fitting these data to Eq. 7. Values for L_C and z_0 are shown in Table 3 for the four different coil geometries studied. As L_0 represents inaccessible inductance, we associate this value with the parasitic inductance of the driving circuit, and assume it is not significantly affected by coil geometry.

Current Sheet	L_C (nH)	z_0 (cm)
CS12	564	2.6
CS20S	624	2.6
CS20L	450	4.0
CS38	558	3.6

Table 3. Fit parameters for various unpinched current sheet geometries.

IV. Expansion of the Model to Two Dimensions

The goal of the development of a two-dimensional expression for inductance is to be able to predict its value at any point in the r-z domain knowing only L_C, z_0, N (a radial fit parameter defined in the next section) and the coil geometry. z_0 and N must be found experimentally. It is possible, yet beyond the scope of this work, that there may be a relation of these parameters to geometry that would obviate experiment altogether.

We begin by estimating the total inductance of a coil as the current sheet undergoes pure radial motion. The data at $z = 0$ is fit well by the function

$$L_{tot}(\bar{r}) = L_0 + L_C \left(1 - \left(\frac{\bar{r}}{\overline{r_{coil}}}\right)^N\right) \tag{10}$$

where $\bar{r}$ is the average radial position of the current sheet

$$\bar{r} = \frac{(R_{cs} - \Delta r) + (r_{cs} - \Delta r)}{2}, \tag{11}$$

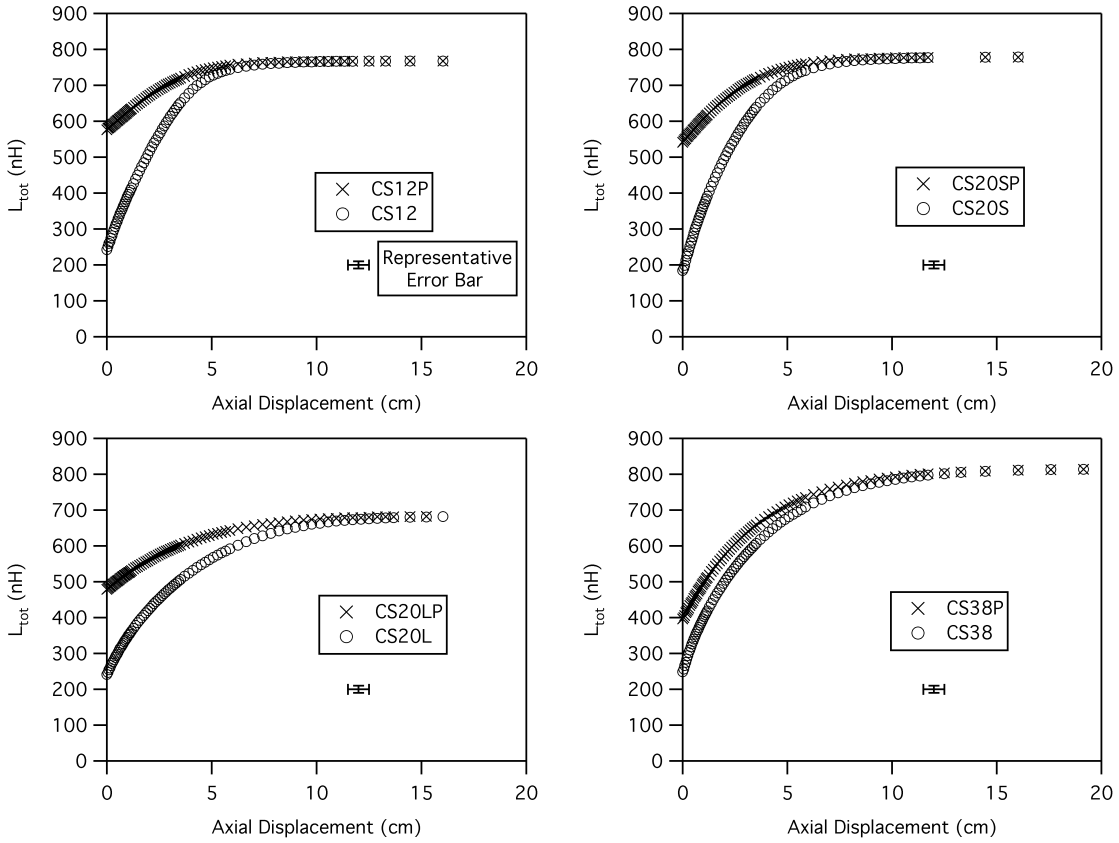

Figure 4. Experimentally measured total inductance for various inductive coil geometries as a function of current sheet displacement with a typical error bar shown. Pinched current sheet trajectories are represented as crosses and unpinched current sheets are represented as circles.

$\overline{r_{coil}}$ is the average radial location of the coil

$$\overline{r_{coil}} = \frac{R_{coil} + r_{coil}}{2}, \tag{12}$$

and N is a parameter that depends on coil geometry. This geometry is shown in the diagram in Fig. 3.

Eq. 10 can be combined with Eq. 7, which is valid for $\bar{r} = \overline{r_{coil}}$, resulting in a function for the two dimensional inductance variation :

$$L_{tot}(r,z) = L_0 + L_C \left(1 - \exp\left(-z/z_0\right)\left(\frac{\bar{r}}{\overline{r_{coil}}}\right)^N\right) \tag{13}$$

The exponent N is found by fitting Eq. 13 to calculations of inductance as a function of radial current sheet compression at zero axial displacement using finite element analysis to create sufficient data points for a fit. These results are shown in Fig. 5 along with a plot of both Eq. 13 and calculations of inductance at an axial displacement of 5 cm.

A comparison of Eq. 13 with experimental data of the coil inductance as a function of simulated pinched current sheet axial displacement is shown in Fig. 6. A comparison of Eq. 13 with calculated and experimental data shows the difference to be well within the error bars.

The model in Section II can be expanded to two dimensions by replacing Eq. 7 with Eq. 13. This leads to a new form for Eq. 8,

$$M = L_C \exp\left(-z/2z_0\right)\left(\frac{\bar{r}}{\overline{r_{coil}}}\right)^{N/2}, \tag{14}$$

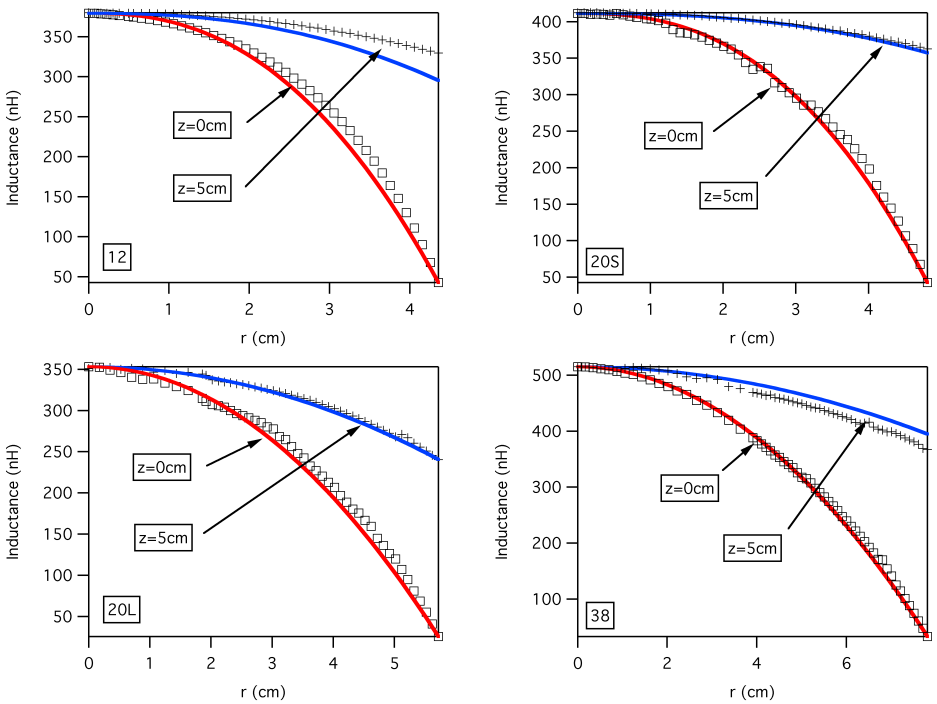

Figure 5. Finite element results of inductance as a function of radial compression of current sheets at two different axial displacements in four different coil geometries. The corresponding function $L_{tot}(r,z)$ is shown as a set of solid lines.

the time evolution of which is now,

$$\frac{dM}{dt} = \frac{L_C}{\overline{r_{coil}}^N}\frac{N}{2}\bar{r}^{\frac{N}{2}-1}\frac{dr}{dt}\exp(-z/z_0) - \frac{L_C}{2z_0}\exp\left(-z/2z_0\right)\frac{dz}{dt}\left(\frac{\bar{r}}{\overline{r_{coil}}}\right)^{N/2}, \tag{15}$$

With a known functional dependence of inductance on both axial and radial position, a momentum equation can now be written for both axial and radial motion :

$$\frac{dv_z}{dt} = \left[\frac{L_C I_1^2}{2z_0}\exp\left(-\frac{z}{z_0}\right)\left(\frac{\bar{r}}{\overline{r_{coil}}}\right)^N\right]/m_{bit}, \tag{16}$$

$$\frac{dv_r}{dt} = \left[-\frac{L_C I_1^2 N}{2\overline{r_{coil}}^N}\exp\left(-\frac{z}{z_0}\right)(\bar{r})^{N-1}\right]/m_{bit}, \tag{17}$$

where v_r is radial velocity. The radial position r is related to the radial velocity by

$$\frac{dr}{dt} = v_r. \tag{18}$$

Eq. 17 is incomplete, however, as it neglects the radial force of the gas-dynamic pressure that, while initially insignificant when compared to the radial Lorentz force, can eventually equal the pressure of the magnetic field accelerating the current sheet.

A. An Estimate of the Gas-dynamic Pressure

An estimate of the gas-dynamic pressure in the propellant of a conical theta pinch pulsed inductive thruster is needed to more accurately represent the radial component of current sheet acceleration. As an upper bound, it is assumed that the current sheet acts as a normal shock wave moving through a volume (defined by the geometry of the current sheet) of propellant, no energy is lost to radiation or ionization, and the total number of particles is constant. The normal shock relation for a calorically perfect gas is:

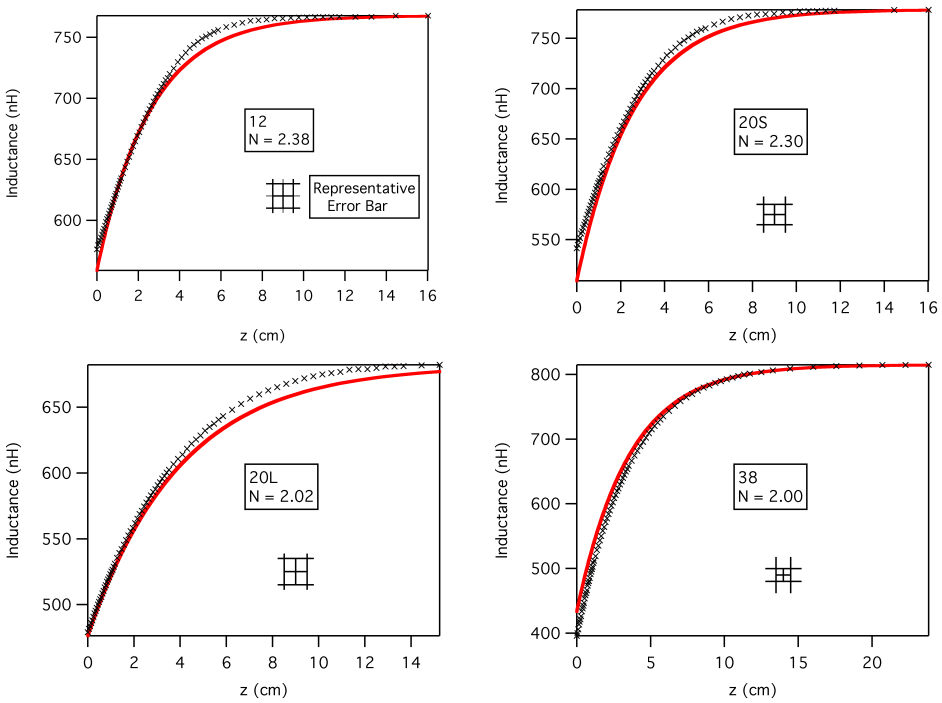

Figure 6. Experimental data of simulated compressed current sheets as a function of axial displacement and the corresponding values of $L_{tot}(r, z)$.

$$\frac{P_2}{P_1} = 1 + \frac{2\gamma}{\gamma + 1}\left[\mathcal{M}^2 - 1\right] \tag{19}$$

where P_2 is the pressure of the gas downstream of the shock, P_1 is the pressure upstream of the shock, γ is the radio of specific heats (taken here to be 5/3), and $\mathcal{M}$ is the local Mach number upstream of the shock:

$$\mathcal{M} = \frac{u}{\sqrt{\frac{\gamma k T_1}{m_i}}} \tag{20}$$

where u is the shock velocity, k is Boltzmann's constant, T_1 is the temperature of the gas upstream of the shock, and m_i is the mass of an ion.

For the parameter space studied here the propellant within the current sheet is initially at room temperature with no imbedded magnetic field, and the only unknowns are the downstream pressure and the shock velocity. If the shock velocity is taken to be the radial current sheet velocity ($u = v_r$), then the downstream pressure of the propellant and its first derivative in time can be calculated as a function of time, and readily incorporated into the two-dimensional circuit model.

The radial force of the gas-dynamic propellant pressure on the current sheet is calculated as:

$$F_P = P_2 2\pi \bar{r} l_{coil} \tag{21}$$

and opposes the Lorentz force in the radial momentum equation (Eq. 17):

$$\frac{dv_r}{dt} = \left[P_f 2\pi \bar{r} l_{coil} - \frac{L_C I_1^2 N}{2\overline{r_{coil}}^N} \exp\left(-\frac{z}{z_0}\right)(\bar{r})^{N-1}\right] / m_{bit}. \tag{22}$$

To calculate the pressure at each time step, the derivative is included in the equation set,

$$\frac{dP_2}{dt} = \frac{P_1 2\gamma}{\gamma + 1}\frac{m_i}{\gamma k T_1} 2 v_r \frac{dv_r}{dt}, \tag{23}$$

bringing the total number of first order ODEs to 9.

V. Model Results and Discussion

Results of the two-dimensional model for the four geometries and parameter space studied here are shown in Fig. 7 along with results from the one-dimensional model where the current sheet does not radially compress. Radial velocities are in the negative r direction, axial velocities are in the positive z direction.

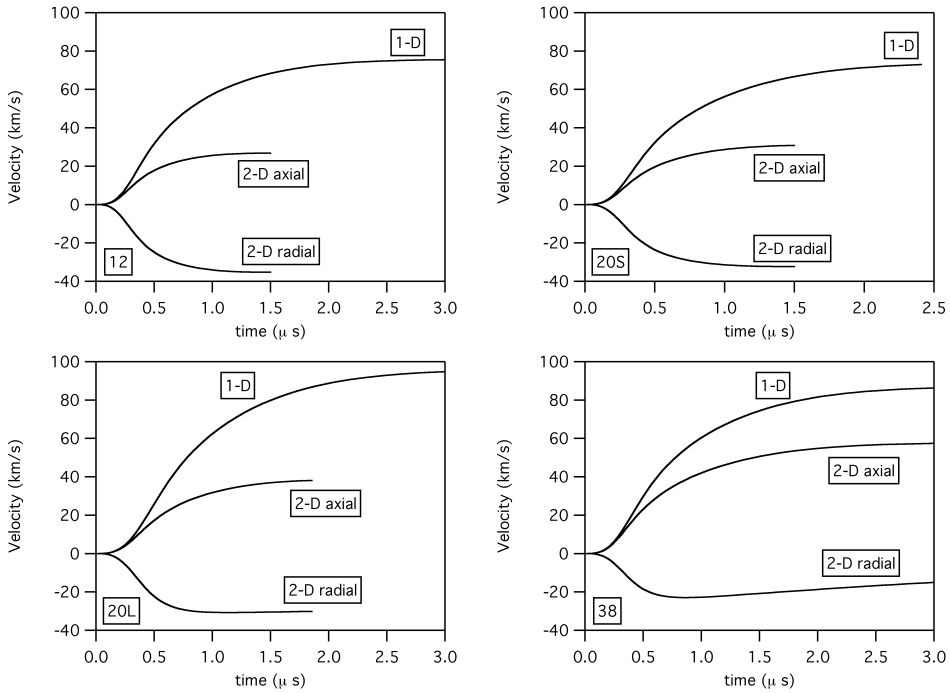

Figure 7. Experimental data of simulated compressed current sheets and the corresponding values of $L_{tot}(r, z)$.

The final axial velocity for the case where the current sheet undergoes radial compression is significantly reduced compared to the case where the current sheet does not undergo radial compression. The final exhaust velocities and their percentage decrease as a consequence of radial compression is shown in Table 4 for the geometries studied.

Geometry	1-D v_z (km/s)	2-D v_z (km/s)	velocity loss	KE loss
12	75	27	64%	87%
20S	73	31	58 %	82%
20L	95	38	60 %	84%
38	86	57	34 %	56%

Table 4. Final exhaust velocities for various current sheet geometries.

It should be noted that we have not included any mechanism in the model for recovery of the energy in the compressed propellant as axial kinetic energy. Although the current sheet is continually accelerated away from any surface upon which a gas-dynamic pressure could be converted to a force, and the operational pressures for a pulsed inductive thruster fall below the range where a physical nozzle could be employed efficiently, we proceed with a calculation of what energy is available due to propellant compression for conversion to axial kinetic energy (irrespective of the conversion mechanism).

The energy E in the compressed propellant is calculated as the gas-dynamic pressure P_2 times the volume $\mathbb{V} = \pi \bar{r}^2 l_{coil}$ to which the current sheet has compressed to achieve this pressure :

$$E = P_2 \pi \bar{r}^2 l_{coil} \tag{24}$$

The maximum calculated amount of recoverable energy E in the compressed propellant available for conversion to axial kinetic energy is shown in Table 5 along with an updated loss in axial kinetic energy with

maximum recovery of gas-dynamic energy. These data demonstrate that the axial directed kinetic energy losses in a conical theta pinch owing to two-dimensional acceleration can be detrimental to overall performance.

Geometry	$P_{max}(Pa)$	$\mathbb{V}$ (m^3)	E_{max} (J)	net E lost (J)
12	8.7e3	2.0e-4	1.7	22.3
20S	1.5e4	3.3e-5	0.44	21.6
20L	1.3e4	3.8e-4	5.1	32.9
38	7.5e3	1.4e-3	2.5	18.5

Table 5. Minimum loss of kinetic energy due to radial current sheet compression.

VI. Conclusions

We have presented the development of a semi-empirical expression for the dependence of coil inductance on current sheet position in two dimensions, and demonstrated its utility by using it to expand a one-dimensional circuit model to two dimensions. The two-dimensional function for coil inductance can be readily adapted to any coil geometry by experimentally determining the values for three parameters (L_C, z_0, and N). It may be possible to relate some of these parameters to geometry, however, an analytic solution does not exist. This two-dimensional function can be tailored to any coil geometry by measuring the inductance as a function of simulated axial current sheet displacement at zero radial displacement, and conversely by measuring the inductance as a function of simulated radial current sheet displacement at zero axial displacement.

Once incorporated into the circuit model, this two-dimensional relation for inductance allows the calculation of axial and radial Lorentz body forces at an averaged current sheet location. With an estimate of how the gas-dynamic pressure of the propellant is affected by current sheet propagation, a radial momentum equation can be written to calculate the radial acceleration of the current sheet. When this model is applied to the parameter space for low power conical pulsed inductive thrusters, the results indicate that radial displacement acts to rapidly decouple the current sheet from the driving coil, leading to a reduced axial kinetic energy as compared to the case of pure axial displacement. An estimation of the available energy in the compressed propellant shows that recovery of lost axial kinetic energy is unlikely.

The range of applicability of these results may extend to all power regimes of this thruster class as the energy conversion process from electrical to thermal and subsequently from thermal to mechanical is necessarily less efficient than a direct electrical to mechanical energy conversion. On the other hand, even if radial compression represents a loss in axial kinetic energy, the extent to which the conical geometry increases the propellant utilization efficiency remains to be explored. These competing effects suggest the existence of an optimum geometry.

Acknowledgments

The authors appreciate the help and support of Dr. Adam Martin, Dr. Noah Rhys, Mr. J. Boise Pearson, and Mr. Jim Martin. This work was supported in part by NASA's Advanced In Space Propulsion Program managed by Dr. Michael LaPointe.

References

[1]Polzin, K. A. Comprehensive review of planar pulsed inductive plasma thruster research and technology. *Journal of Propulsion and Power*, 27(3):513–531, May-June 2011.

[2]Lovberg, R. H. and Dailey, C. L. A PIT primer. Technical Report 005, RLD Associates, Encino, CA, 1994.

[3]Dailey, C. L. and Lovberg, R. H. The PIT MkV Pulsed Inductive Thruster. Technical Report 191155, Lewis Research Center, Redondo Beach, CA, July 1993.

[4]Polzin, K. A. Rose, M. F. and Miller, R. Operational Characteristics of a Low-Energy FARAD Thruster. Number AIAA 2008-5011, July 2008.

[5]Eskridge, R. H. Martin, A. K. Electrical coupling efficiency of inductive plasma accelerators. *Journal of Physics D: Applied Physics*, 38:4168–4179, December 2005.

[6]Bernardes, J. Merryman, S. Rose, M. F. and Martin, T. H. Parameter Analysis of a Single Stage Induction Mass Driver. Technical report, 5th IEEE Int. Pulsed Power conf.

[7]Hallock, A. K. Polzin, K. A. and Emsellem, G. D. Effect of Inductive Coil Geometry and Current Sheet Trajectory of a Conical Theta Pinch Pulsed Inductive Plasma Accelerator. Number AIAA-2011-6068, August 2011.

Two-dimensional Analysis of Conical Pulsed Inductive Plasma Thruster Performance

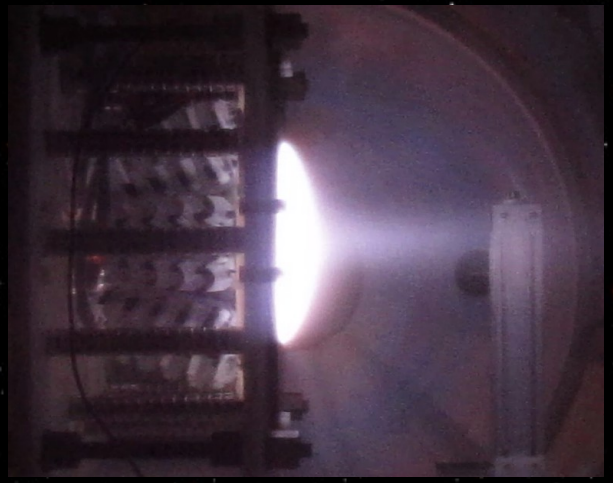

Ashley Hallock

Princeton University

Kurt Polzin

NASA MSFC

Gregory Emsellem

The Elwing Company

International Electric Propulsion Conference

Wiesbaden, Germany

11-15 September 2011

Outline of Talk

- Low Power Pulsed Inductive Plasma Thrusters
- Semi-empirical Model
  - Circuit model coupled to 1-D momentum equation
- Experiment
  - Simulating current sheet trajectories
- Expansion of Model to 2-D
  - L(r,z)
  - Estimate of time-changing gas-dynamic pressure
- Model Results
- Conclusions

Pulsed Inductive Plasma Thrusters

Pulsed Inductive Plasma Thrusters

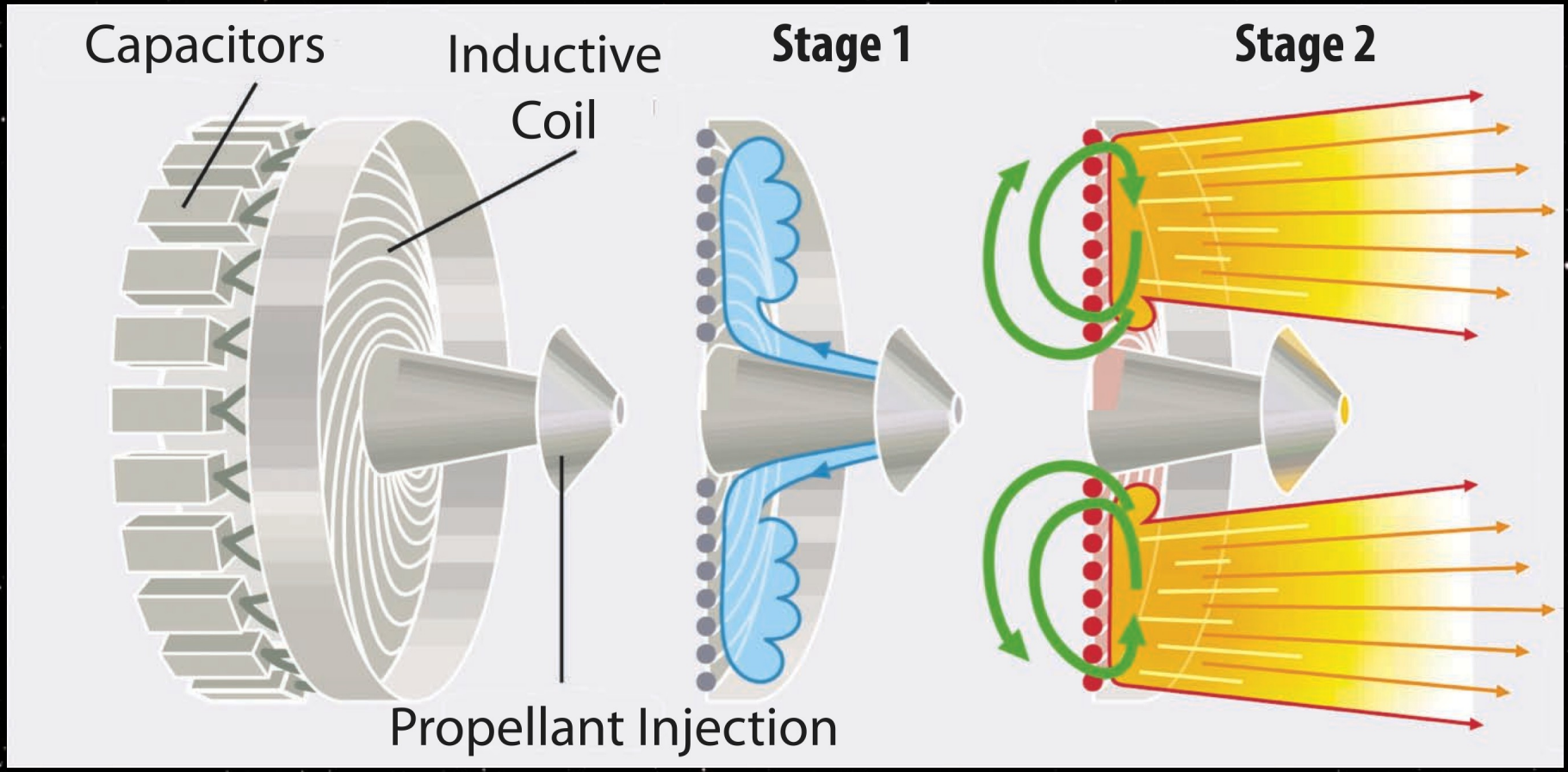

Microwave Assisted Discharge Inductive Plasma Accelerator

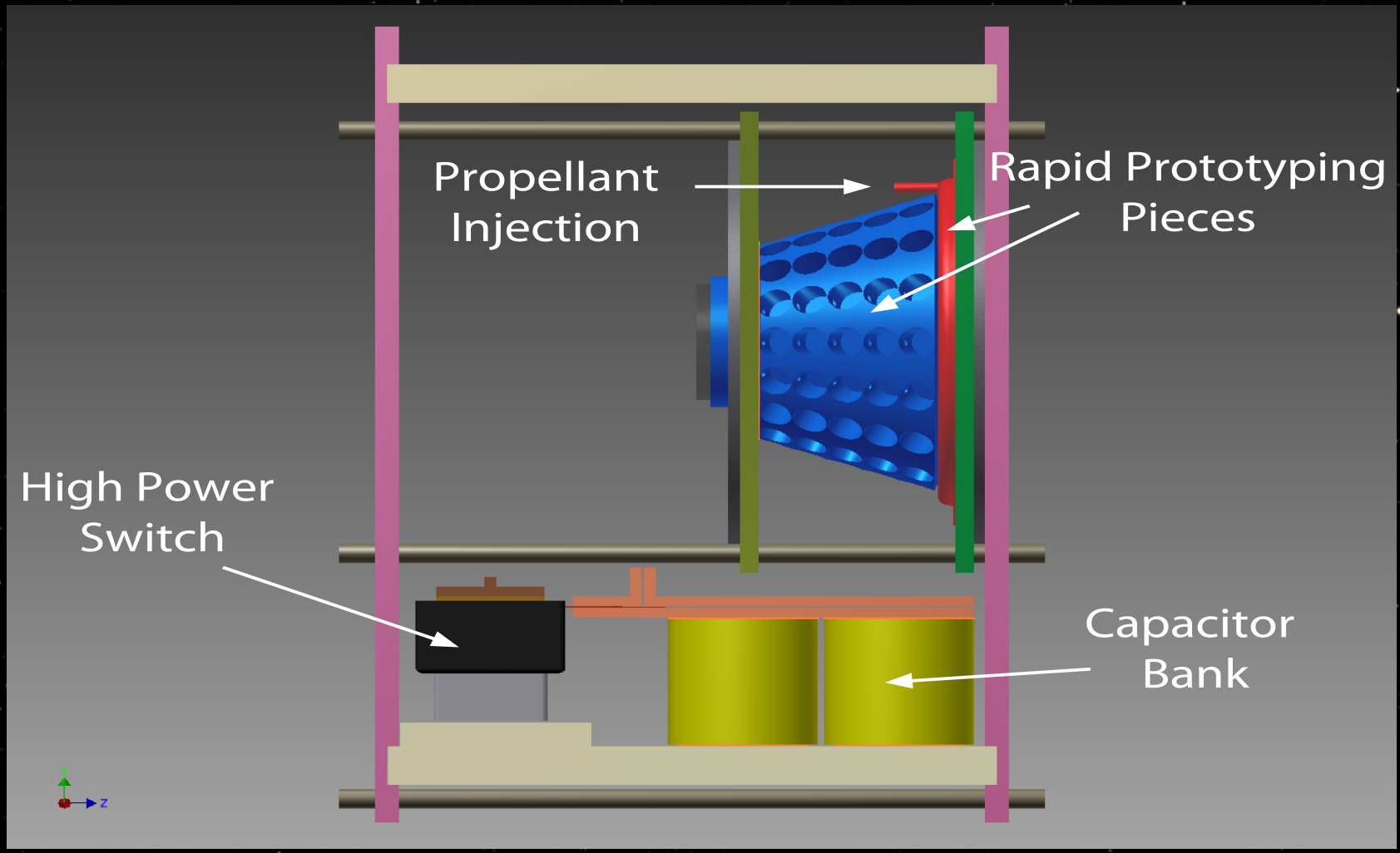

Microwave Assisted Discharge Inductive Plasma Accelerator

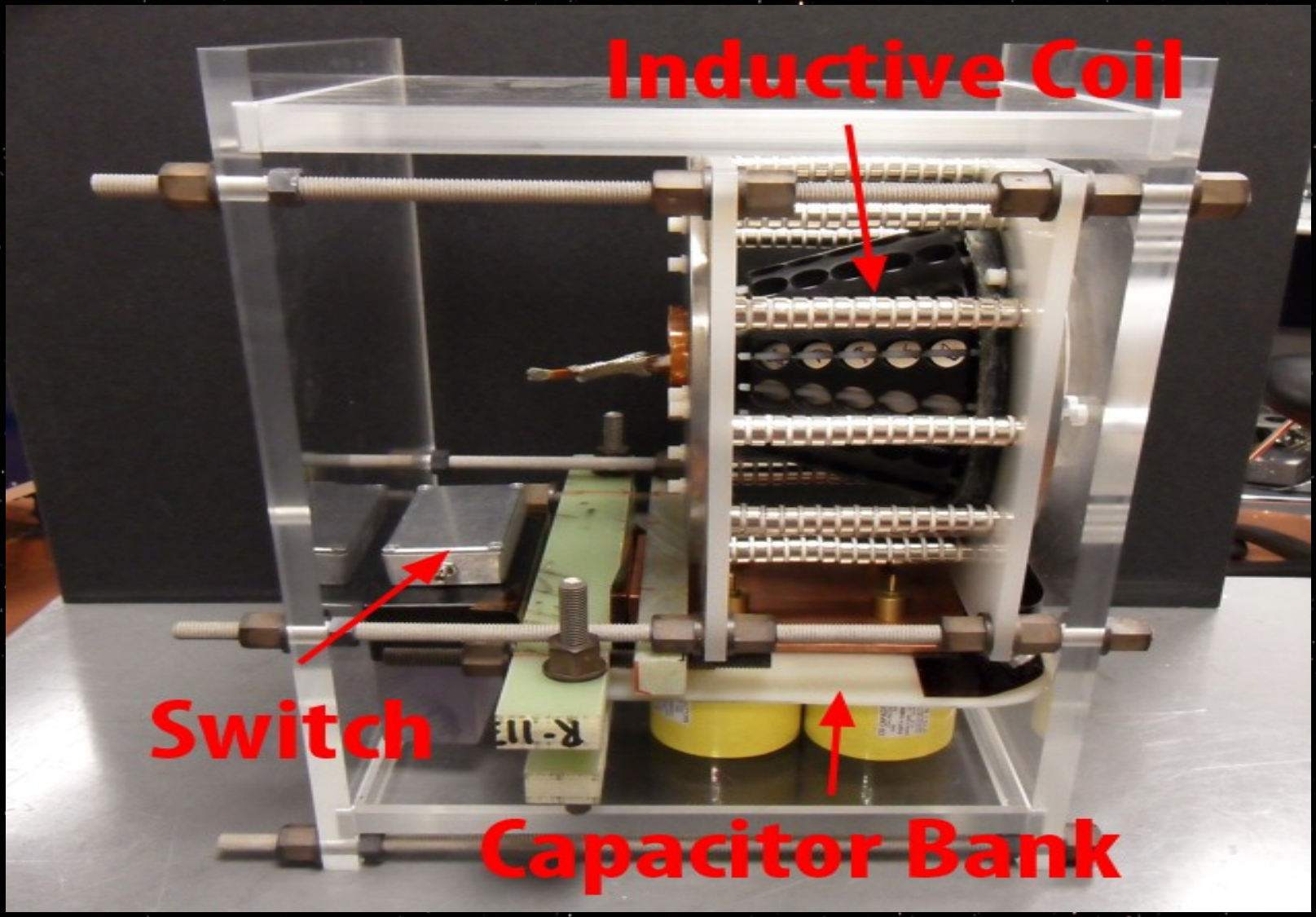

Mounted on VAHPER Thrust Stand

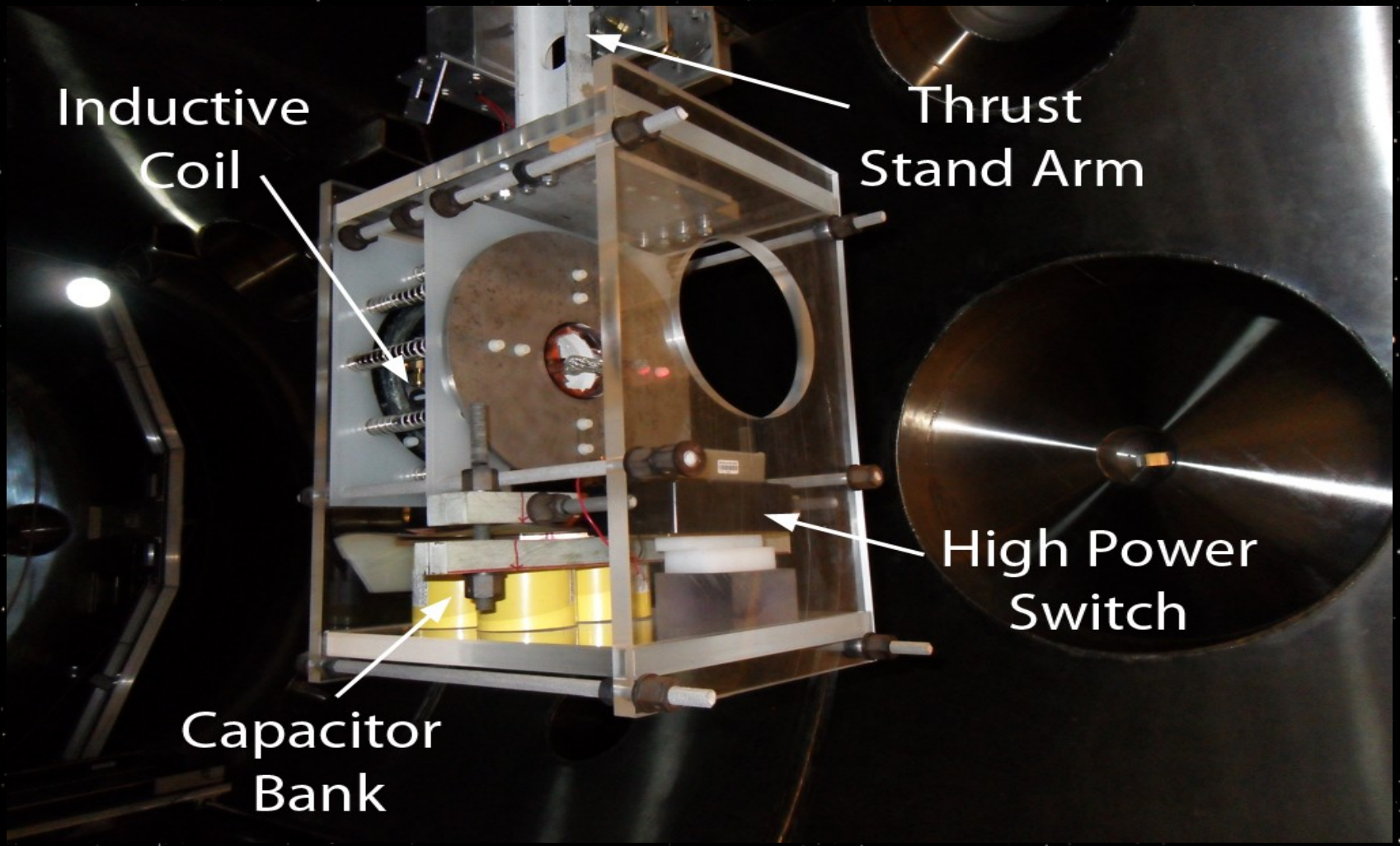

Mounted on VAHPER Thrust Stand

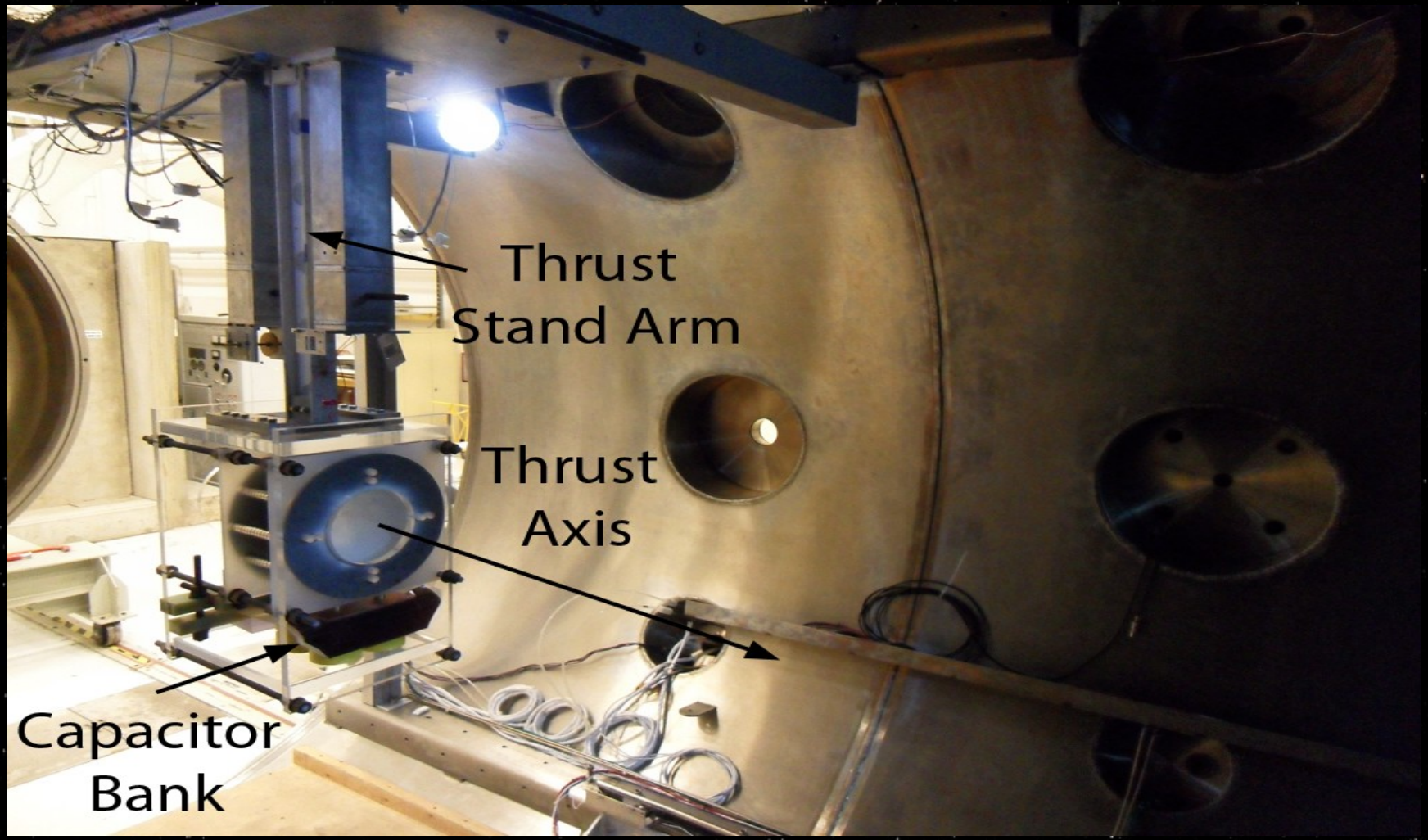

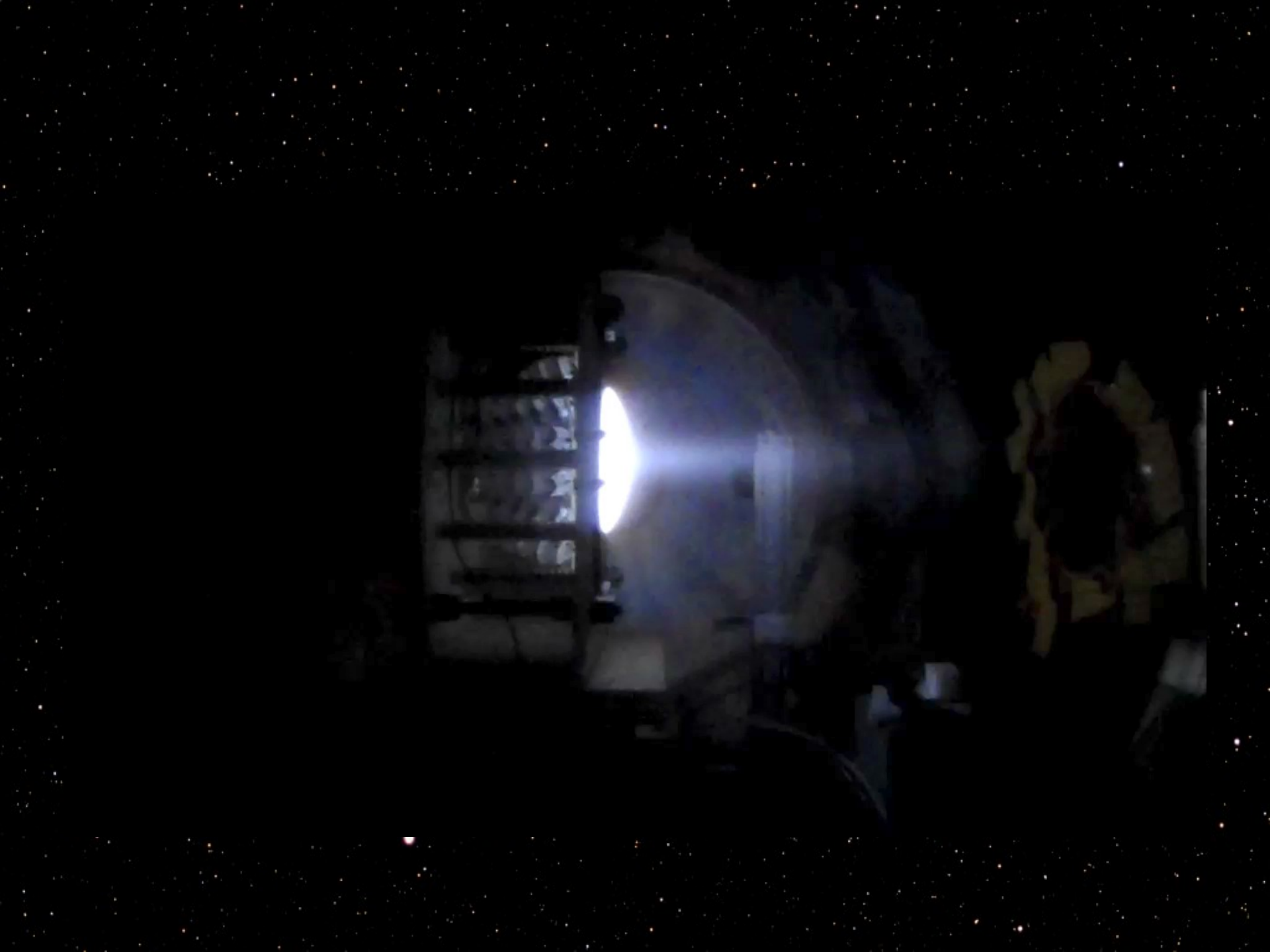

Semi-empirical Model

Lumped-element Circuit Model

L_0 is INACCESSIBLE inductance

L_C is ACCESSIBLE inductance

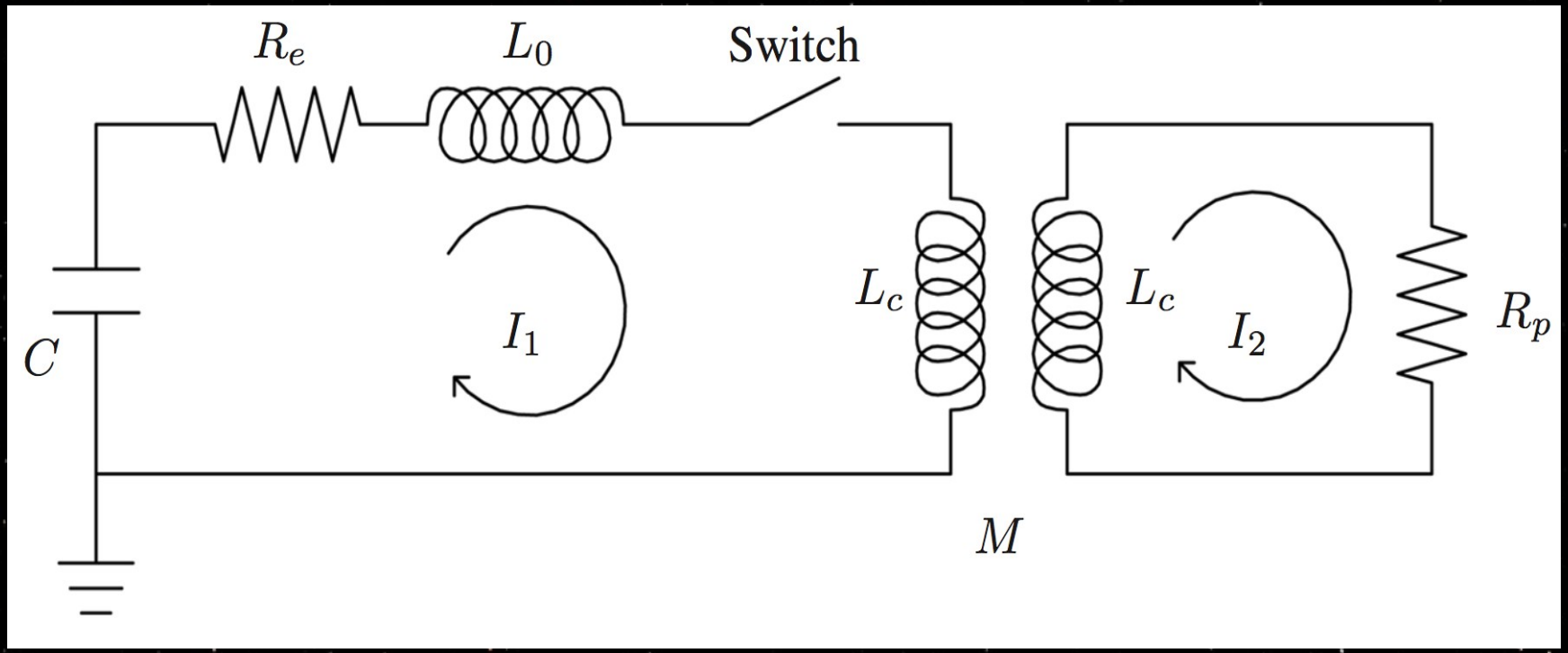

Equivalent Circuit

L_0 is INACCESSIBLE inductance

L_c is ACCESSIBLE inductance

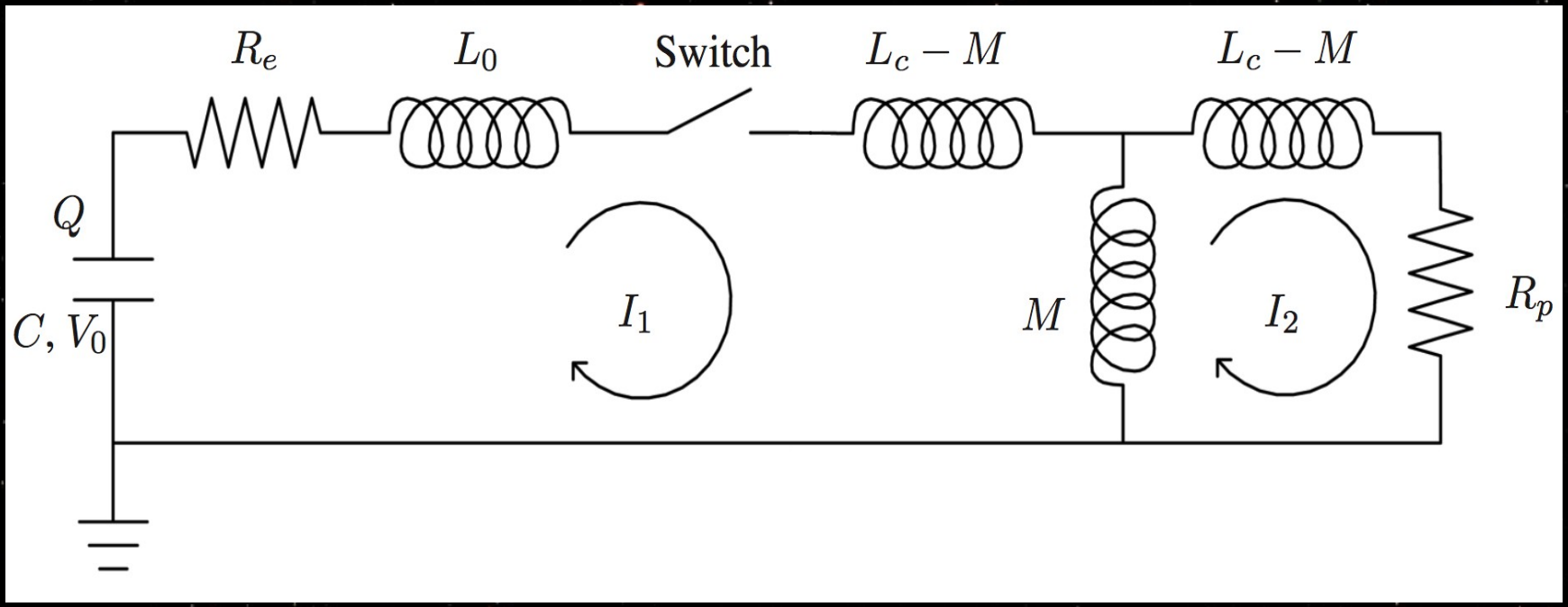

Circuit Analysis Gives 3 Coupled ODEs

$$\frac{dI_1}{dt} = \frac{L_C V - L_C R_e I_1 - M R_p I_2 + (L_C I_2 + M I_1)\frac{dM}{dt}}{L_C\left(L_0 + L_C\right) - M^2}$$

$$\frac{dI_2}{dt} = \frac{M\frac{dI_1}{dt} + I_1\frac{dM}{dt} - R_p I_2}{L_C}$$

$$\frac{dV}{dt} = \frac{-I_1}{C}$$

Empirical Inductance Relation : Axial

$$L_{tot} = L_0 + L_C - \frac{M^2}{L_C}$$

$$L_{tot}(z) = L_0 + L_C\left(1 - \exp\left(-z/z_0\right)\right)$$

$$M = L_C \exp\left(-z/2z_0\right)$$

$$\frac{dM}{dt} = -\frac{L_C}{2z_0} \exp\left(-z/2z_0\right) \frac{dz}{dt}$$

Momentum Equation for Current Sheet Slug Motion

$$\frac{dz}{dt} = v_z$$

$$\frac{dv_z}{dt} = \frac{L_C I_1^2}{2 z_0 m_{bit}} \exp\left(-\frac{z}{z_0}\right)$$

- Only taking into account direct axial electromagnetic acceleration
- Uses equation for L_{tot}

Experiment

Four Coil Geometries and Eight Current Sheet Geometries

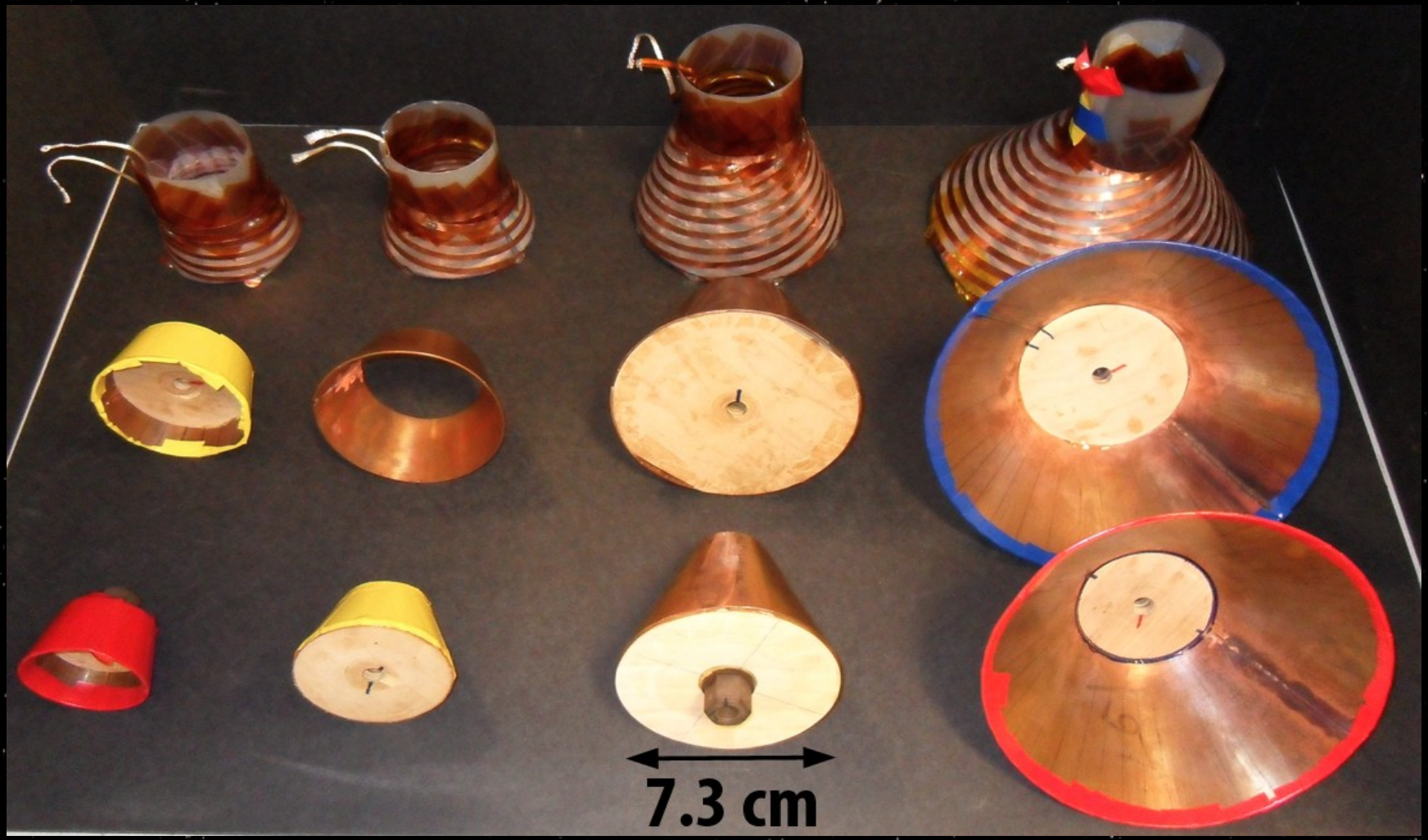

Four Coil Geometries and Eight Current Sheet Geometries

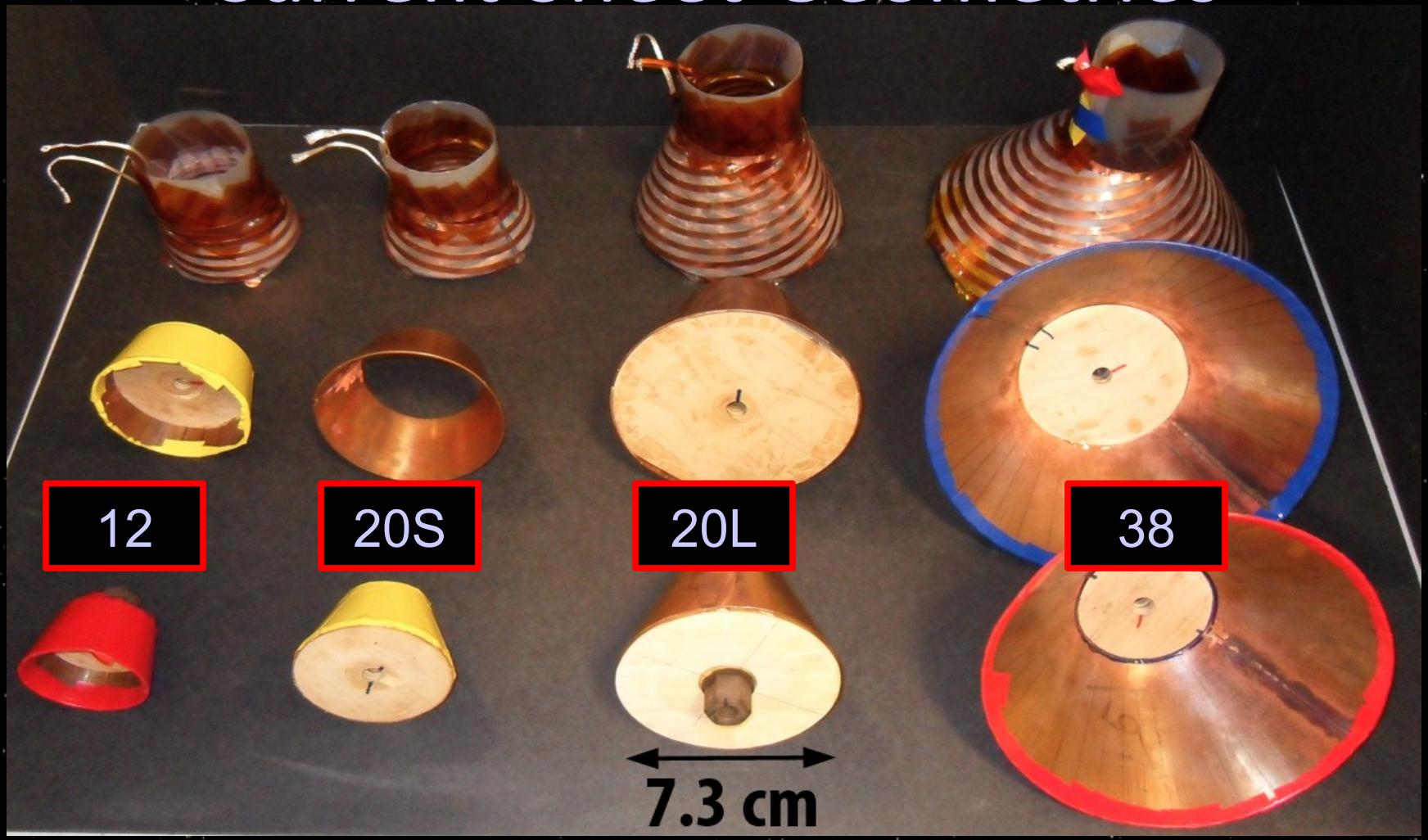

Two Current Sheets for Every Coil

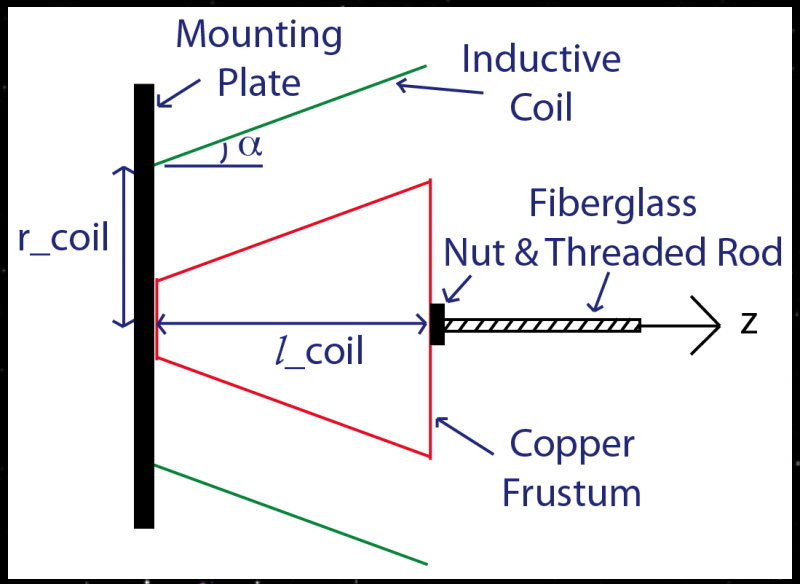

$z=z_0$

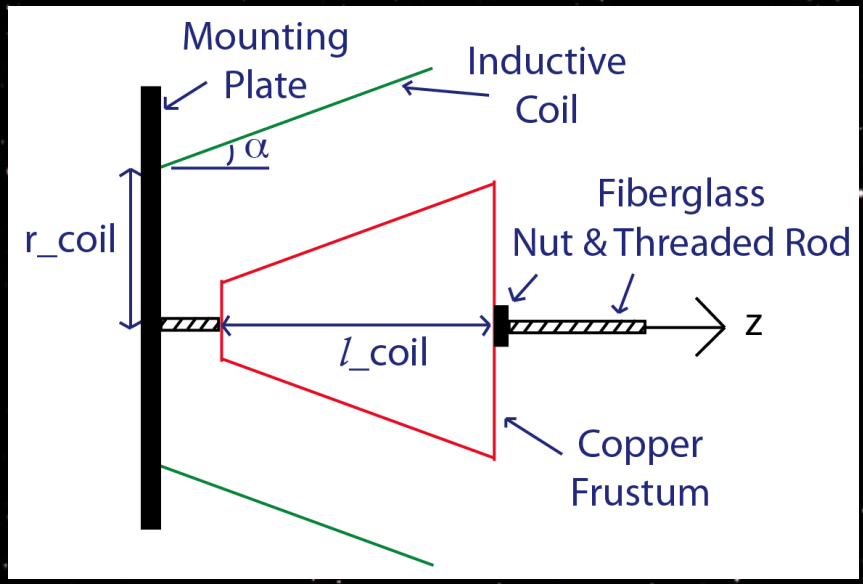

$z=2*z_0$

Experimental Results

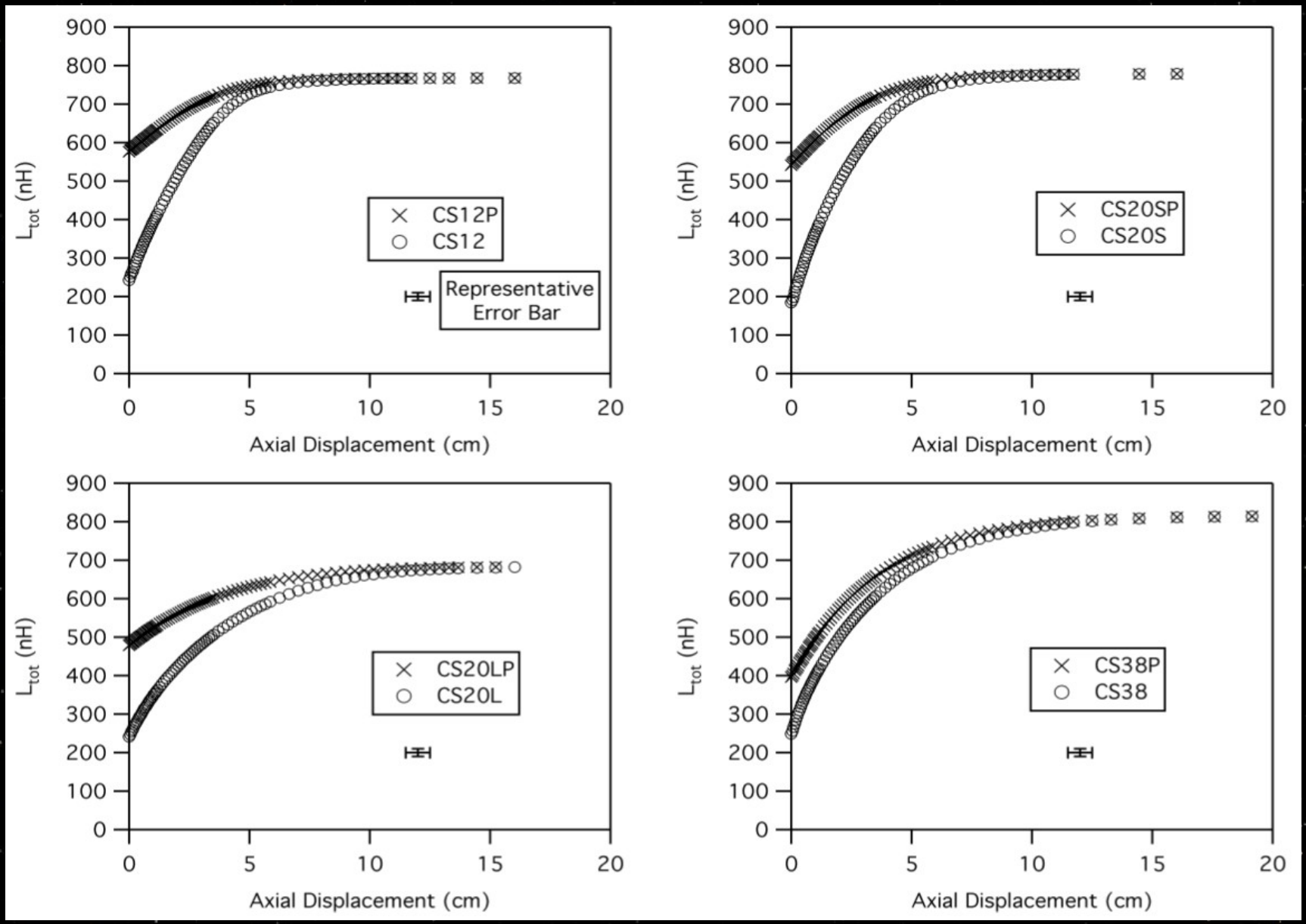

Data of Wide Geometry Range Fit Model Well

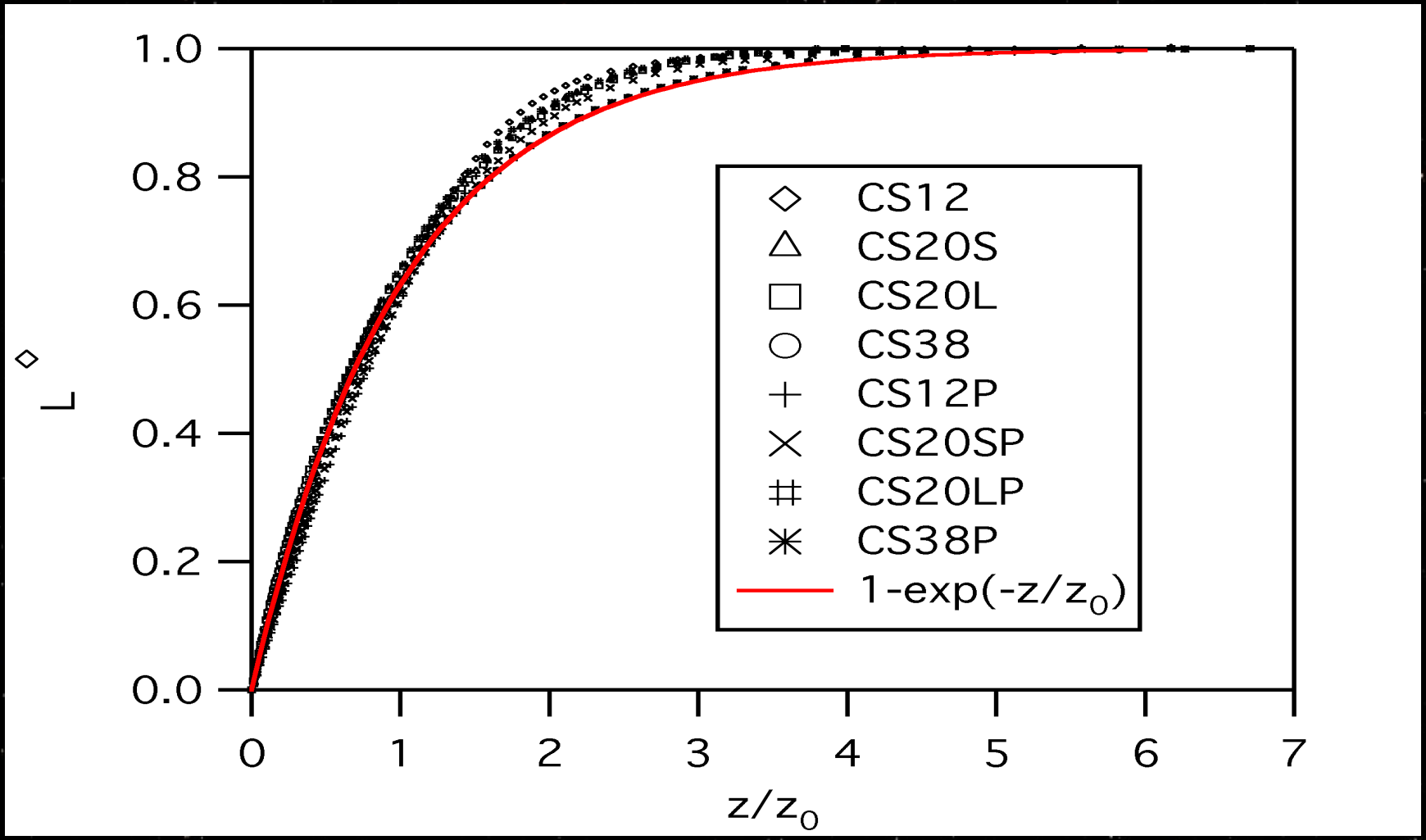

Loss of Shielded Volume in Pinched Current Sheets

No Radial Displacement
No Axial Displacement

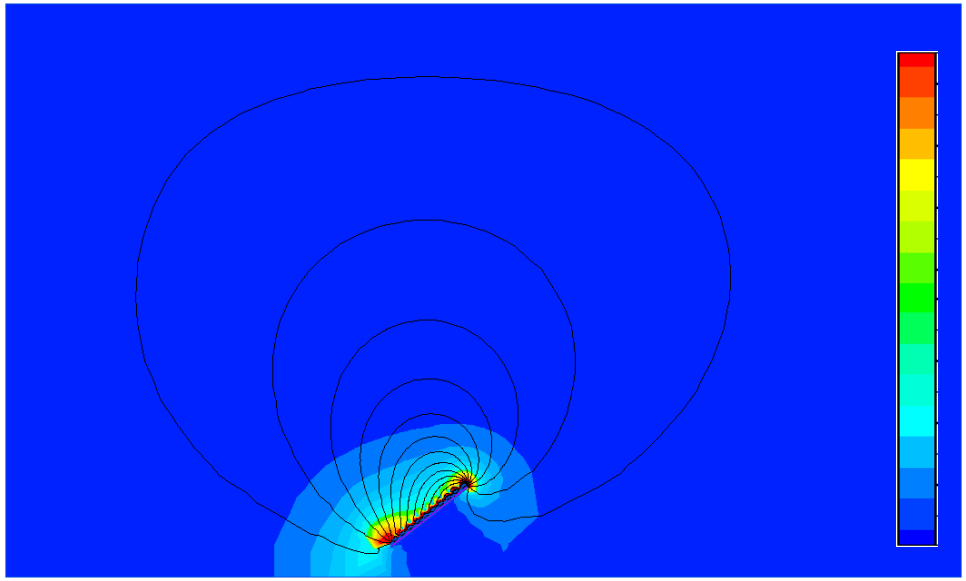

36% Radial Displacement
No Axial Displacement

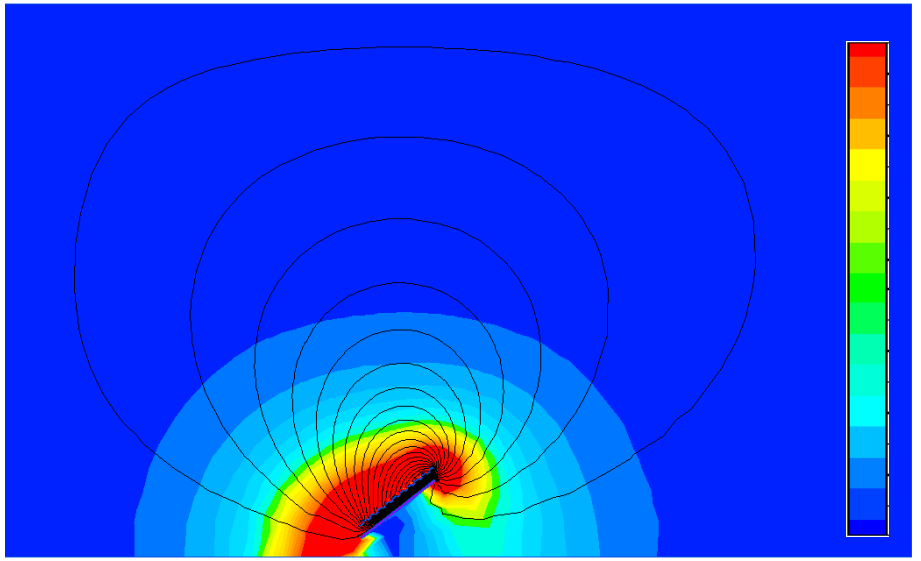

Thruster Efficiency Relies on Large Shielded Volume

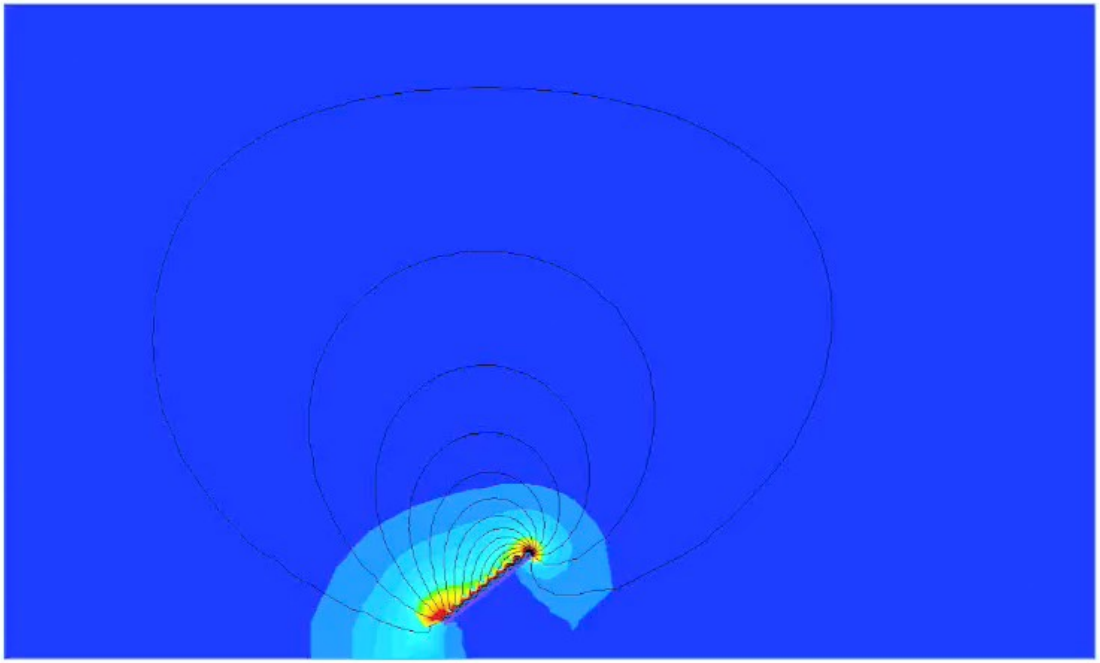

Expansion of the Model to 2-D

Finite Element Analysis of Radial Inductance Profile

- L(r,z=0)

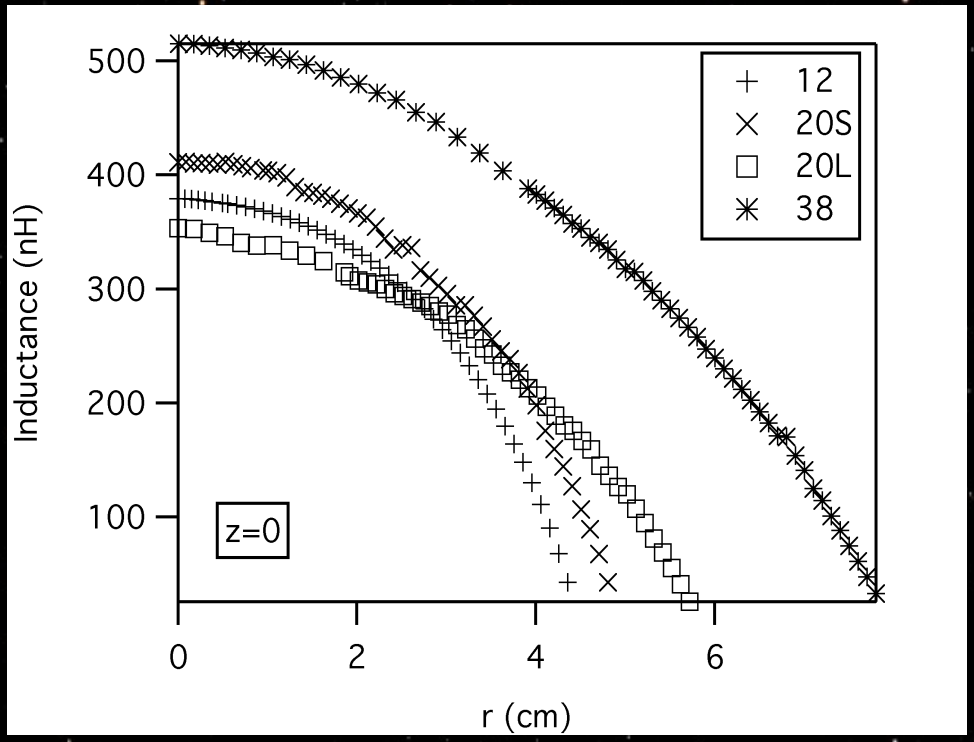

Radial Inductance Profile Equation

L(r,z=0)

$$L_{tot}(\bar{r}) = L_0 + L_C \left(1 - \left(\frac{\bar{r}}{\overline{r_{coil}}}\right)^N\right)$$

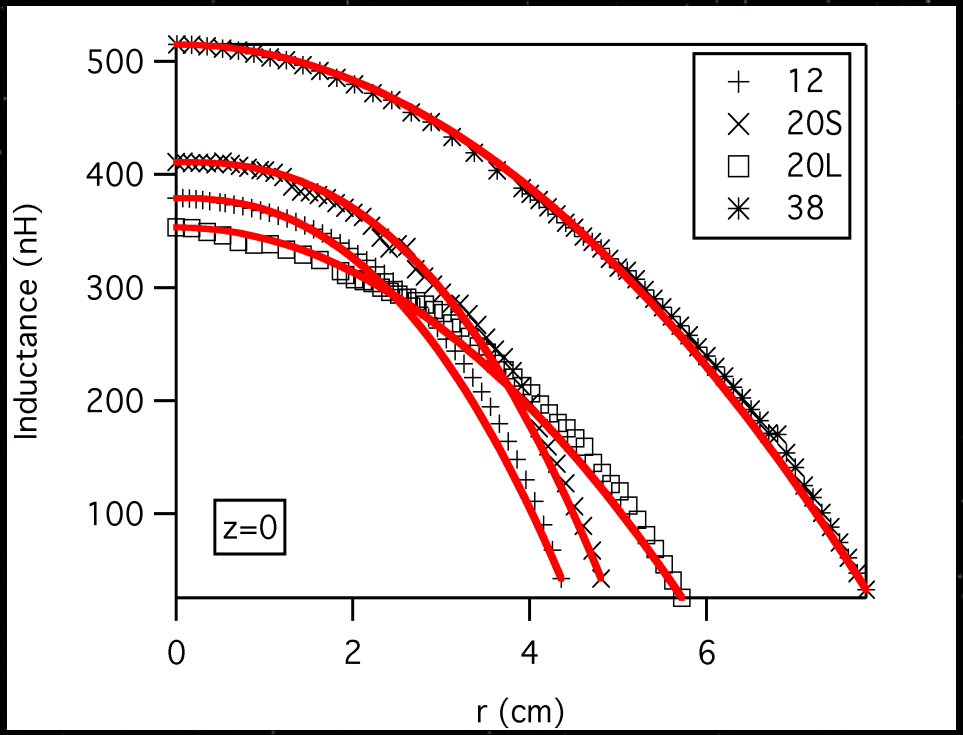

$$\overline{r_{coil}} = \frac{R_{coil} + r_{coil}}{2}$$

$$\bar{r} = \frac{R_{coil} - \Delta r + r_{coil} - \Delta r}{2}$$

Combination of Radial & Axial Inductance Profile

$$L_{tot}(\bar{r}) = L_0 + L_C \left(1 - \left(\frac{\bar{r}}{r_{coil}}\right)^N\right)$$

$$L_{tot}(z) = L_0 + L_C \left(1 - \exp\left(-z/z_0\right)\right)$$

$$L_{tot}(r,z) = L_0 + L_C \left(1 - \exp\left(-z/z_0\right)\left(\frac{\bar{r}}{r_{coil}}\right)^N\right)$$

Comparison to Finite Element Analysis Results at z=0 & z=5cm

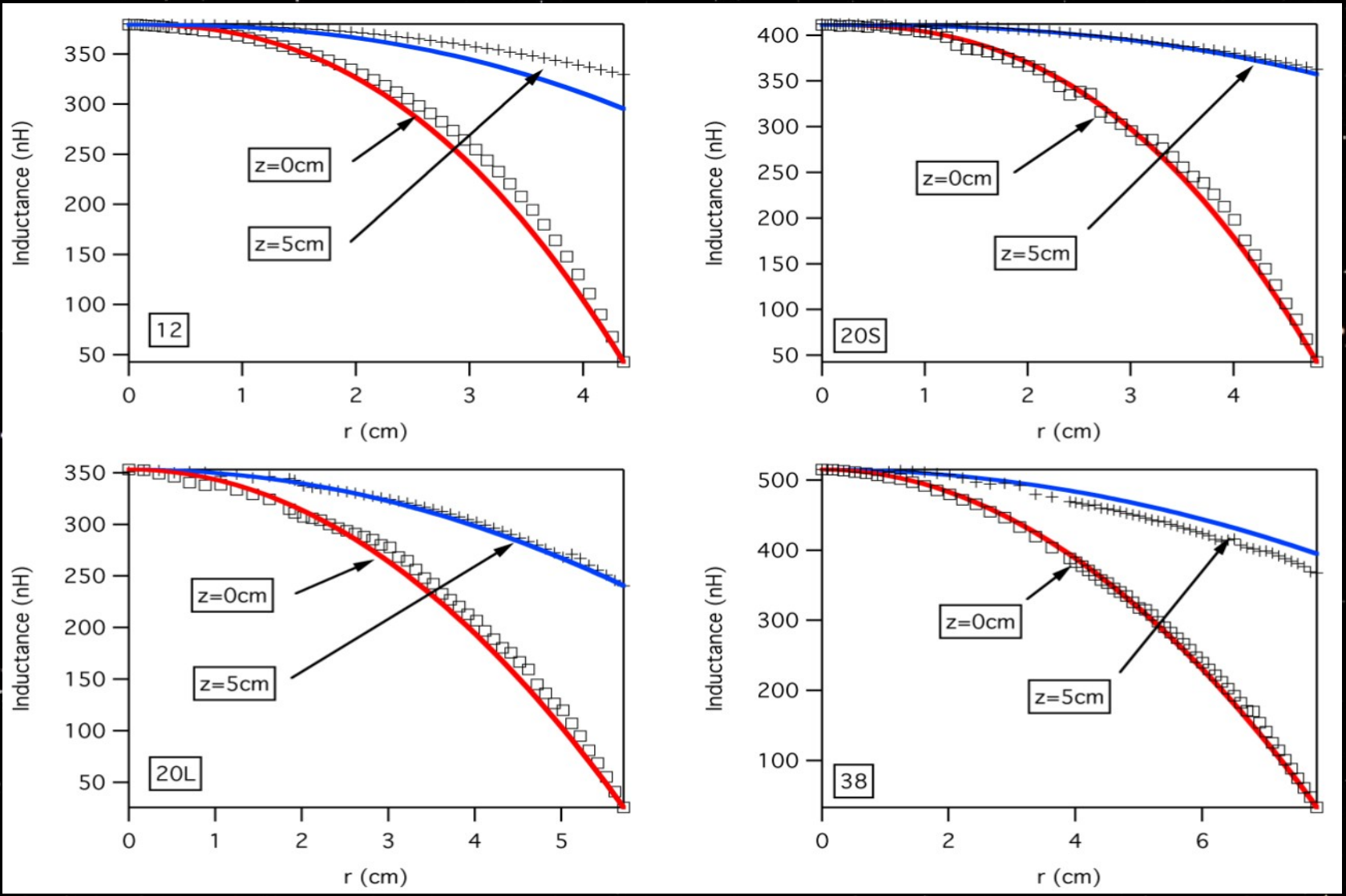

Expansion of Model to 2-D

$$L_{tot}(r,z) = L_0 + L_C\left(1 - \exp\left(-z/z_0\right)\left(\frac{\bar{r}}{r_{coil}}\right)^N\right)$$

$$M = L_C \exp\left(-z/2z_0\right)\left(\frac{\bar{r}}{r_{coil}}\right)^{N/2}$$

$$\frac{dM}{dt} = \frac{L_C}{r_{coil}{}^N}\frac{N}{2}\bar{r}^{\frac{N}{2}-1}\frac{dr}{dt}\exp(-z/z_0) - \frac{L_C}{2z_0}\exp\left(-z/2z_0\right)\frac{dz}{dt}\left(\frac{\bar{r}}{r_{coil}}\right)^{N/2}$$

Radial & Axial Momentum Equations

- Force is derived from gradient in L

$$\frac{dv_z}{dt} = \left[\frac{L_C I_1^2}{2z_0} \exp\left(-\frac{z}{z_0}\right) \left(\frac{\bar{r}}{\overline{r_{coil}}}\right)^N \right] / m_{bit}$$

$$\frac{dv_r}{dt} = \left[-\frac{L_C I_1^2 N}{2\overline{r_{coil}}^N} \exp\left(-\frac{z}{z_0}\right) (\bar{r})^{N-1} \right] / m_{bit}$$

Radial & Axial Momentum Equations

- Force is derived from gradient in L

$$\frac{dv_z}{dt} = \left[\frac{L_C I_1^2}{2z_0} \exp\left(-\frac{z}{z_0}\right) \left(\frac{\bar{r}}{\overline{r_{coil}}}\right)^N \right] / m_{bit}$$

$$\frac{dv_r}{dt} = \left[-\frac{L_C I_1^2 N}{2\overline{r_{coil}}^N} \exp\left(-\frac{z}{z_0}\right) (\bar{r})^{N-1} \right] / m_{bit}$$

- Radial pressure force missing

Upper Estimate of Gas-dynamic Propellant Pressure

- Constant number of particles
- Current sheet acts as a normal shock wave
- No radiation losses

$$\frac{P_2}{P_1} = 1 + \frac{2\gamma}{\gamma + 1}\left[\mathcal{M}^2 - 1\right]$$

$$\mathcal{M} = \frac{u}{\sqrt{\frac{\gamma k T_1}{m_i}}}$$

$$\frac{dP_2}{dt} = \frac{P_1 2\gamma}{\gamma + 1}\frac{m_i}{\gamma k T_1} 2 v_r \frac{dv_r}{dt}$$

Radial Magnetic and Gas-dynamic Force Balance

$$F_P = P_2 2\pi \bar{r} l_{coil}$$

$$F_L = -\frac{L_C I_1^2 N}{2\overline{r_{coil}}^N} \exp\left(-\frac{z}{z_0}\right) (\bar{r})^{N-1}$$

$$\frac{dv_r}{dt} = \frac{\left[P_2 2\pi \bar{r} l_{coil} - \frac{L_C I_1^2 N}{2\overline{r_{coil}}^N} \exp\left(-\frac{z}{z_0}\right) (\bar{r})^{N-1}\right]}{m_{bit}}$$

Model Results

Model Results for 1-D and 2-D motion

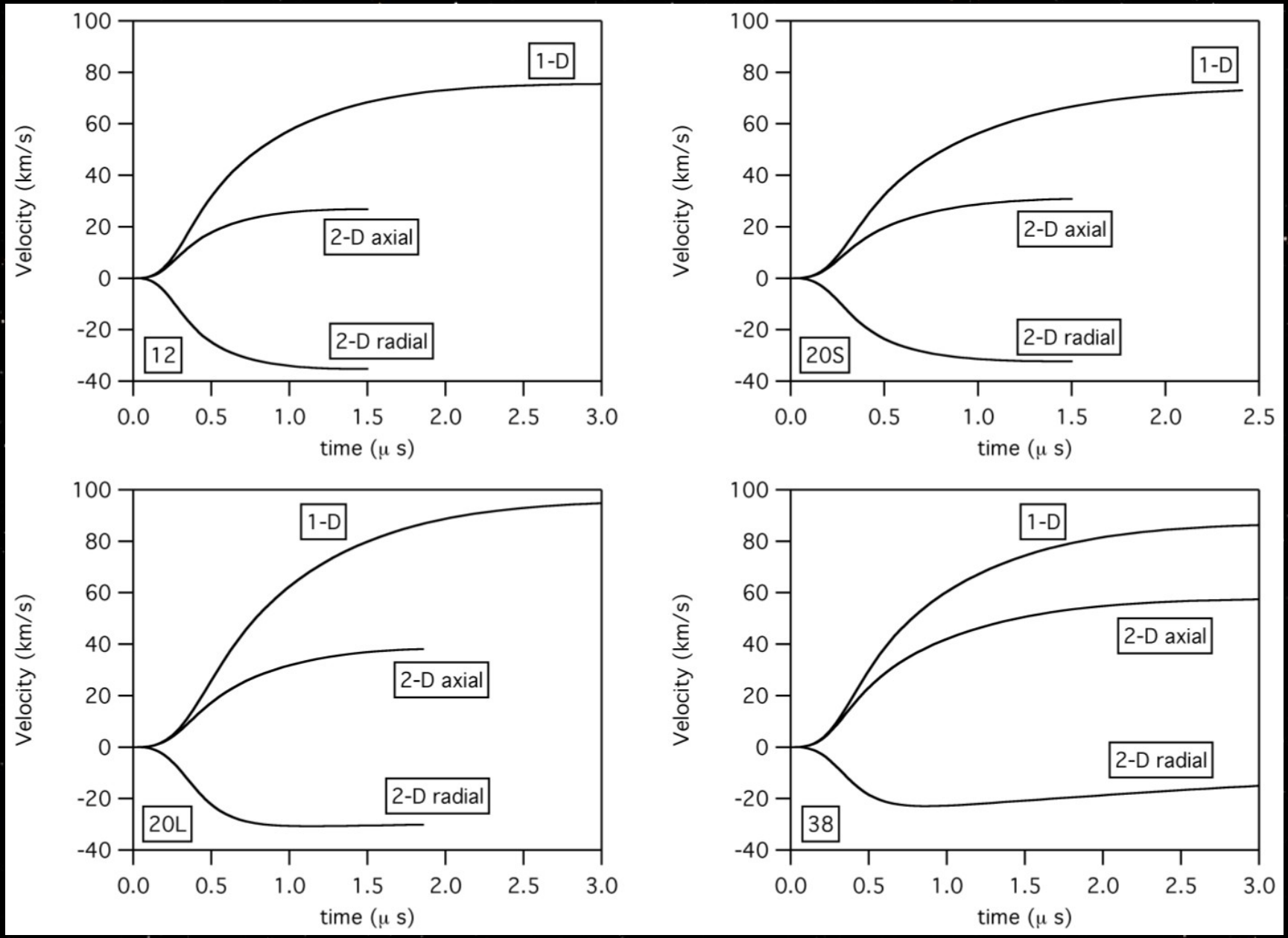

KE Loss and Recovery Analysis

Geometry	1-D v_z (km/s)	2-D v_z (km/s)	velocity loss	KE loss
12	75	27	64%	87%
20S	73	31	58 %	82%
20L	95	38	60 %	84%
38	86	57	34 %	56%

KE Loss and Recovery Analysis

Geometry	1-D v_z (km/s)	2-D v_z (km/s)	velocity loss	KE loss
12	75	27	64%	87%
20S	73	31	58 %	82%
20L	95	38	60 %	84%
38	86	57	34 %	56%

$$E = P_2 \pi \bar{r}^2 l_{coil}$$

KE Loss and Recovery Analysis

Geometry	1-D v_z (km/s)	2-D v_z (km/s)	velocity loss	KE loss
12	75	27	64%	87%
20S	73	31	58 %	82%
20L	95	38	60 %	84%
38	86	57	34 %	56%

$$E = P_2 \pi \bar{r}^2 l_{coil}$$

Geometry	$P_{max}(Pa)$	$\mathbb{V}$ (m^3)	E_{max} (J)	net E lost (J)	% KE loss
12	8.7e3	2.0e-4	1.7	22.3	80%
20S	1.5e4	3.3e-5	0.44	21.6	80%
20L	1.3e4	3.8e-4	5.1	32.9	73%
38	7.5e3	1.4e-3	2.5	18.5	50%

Conclusions

- 2-D semi-empirical relation for inductance fits data well
- Expansion to 2-D circuit model yields useful insight
- Current sheet radial displacement decreases accessible inductance and, in turn, achievable direct axial acceleration
- Energy in compressed propellant insufficient to compensate for this axial KE loss
- Results may also apply to thrusters of higher power
- Effect of geometry on propellant utilization efficiency remains unexplored : optimum geometry

Acknowledgments

- The authors appreciate the help and support of Dr. Adam Martin, Dr. Noah Rhys, Mr. J. Boise Pearson, and Mr. Jim Martin.
- This work was supported in part by NASA's Advanced In Space Propulsion Program managed by Dr. Michael LaPointe.

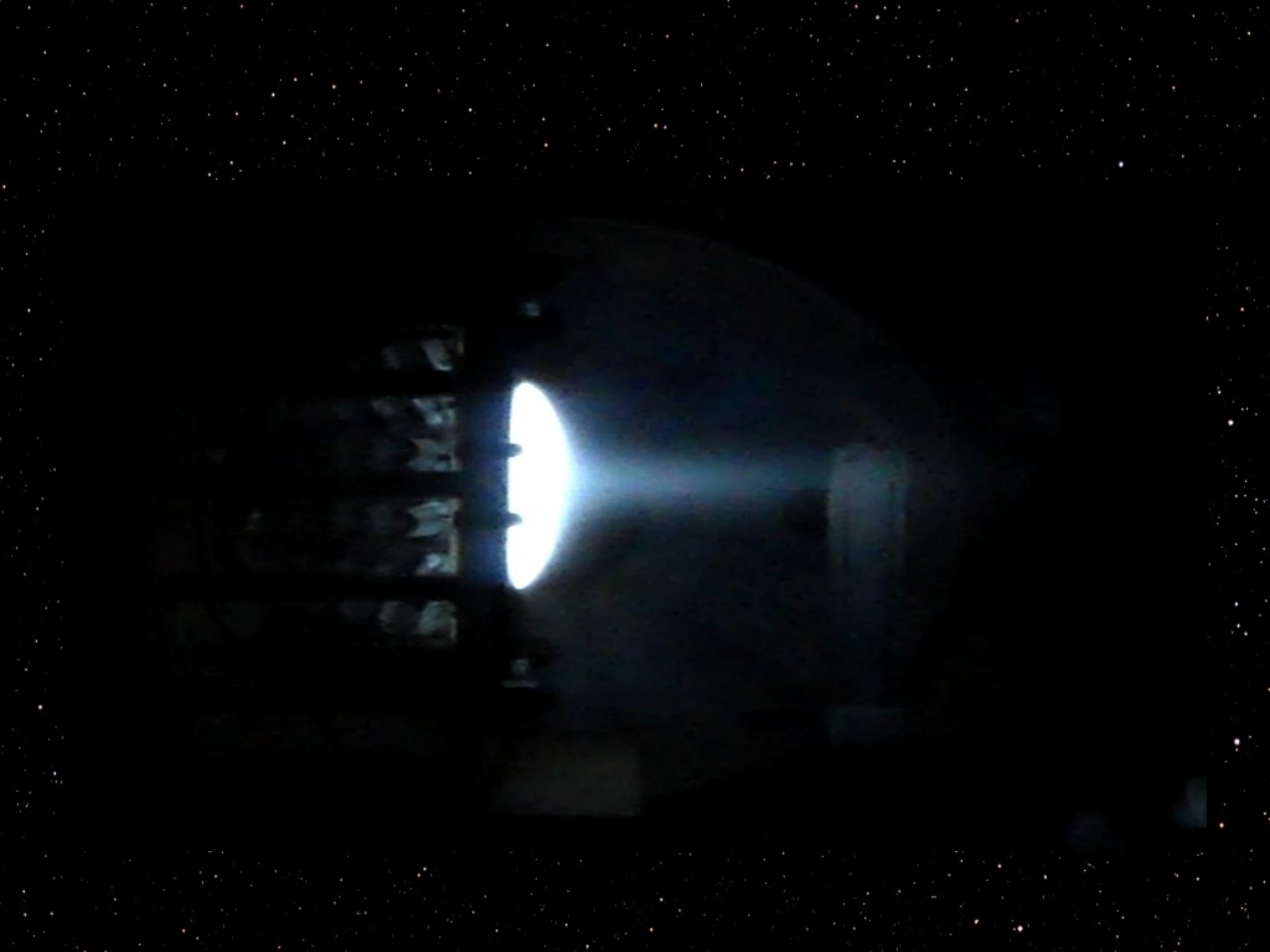

FRCs

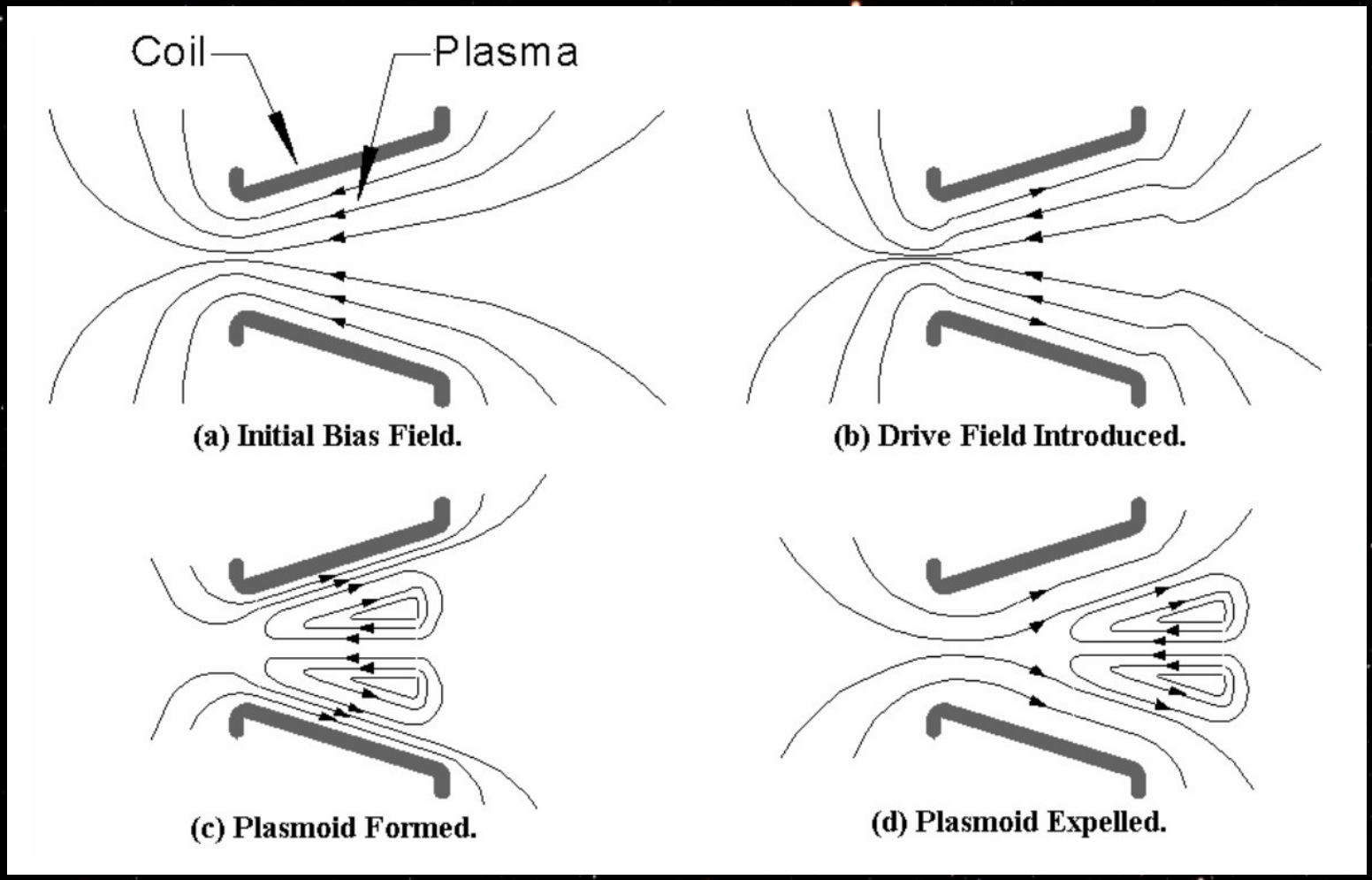
Coil
Plasma
(a) Initial Bias Field.
(b) Drive Field Introduced.
(c) Plasmoid Formed.
(d) Plasmoid Expelled.

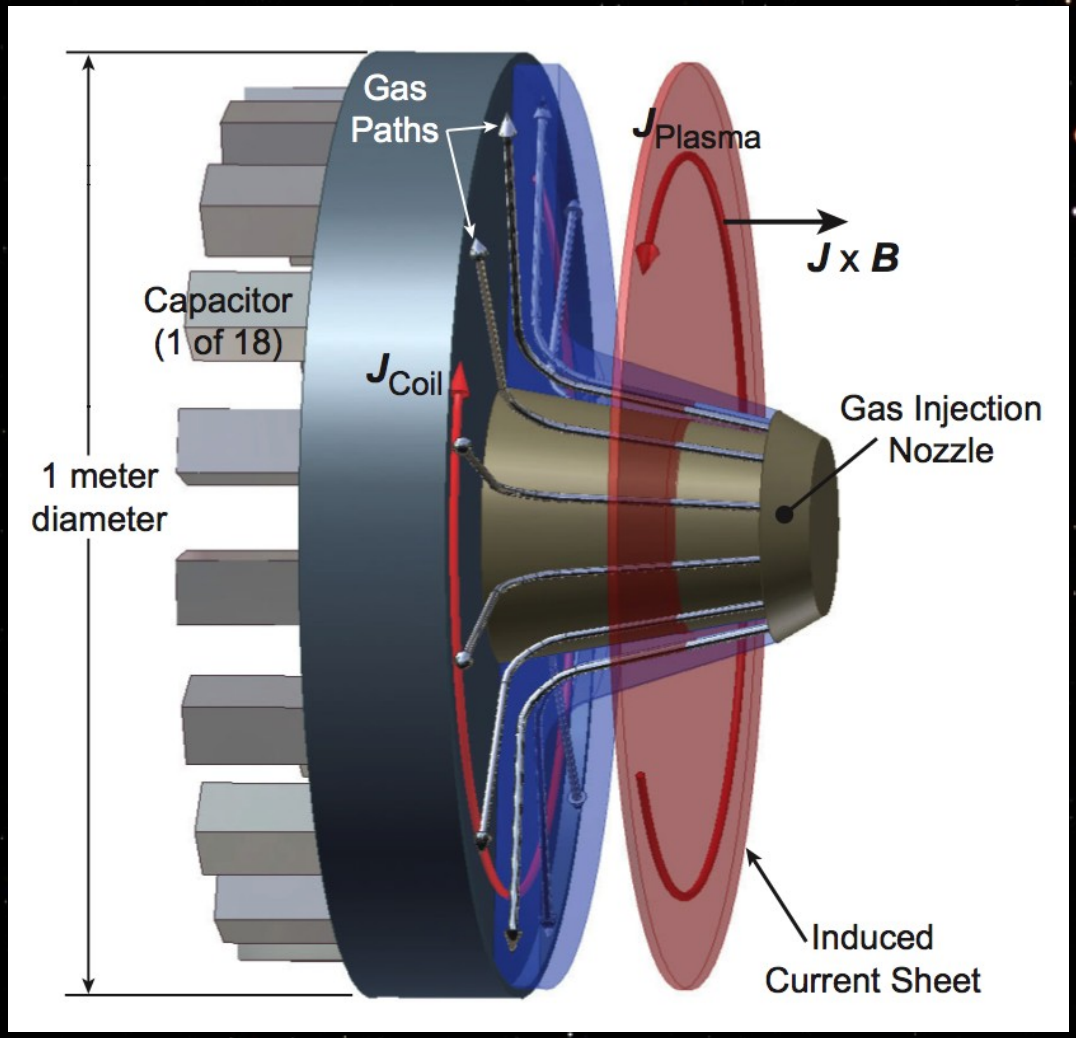

- Electrodeless
- 15 kV capacitor charging
- 30 kV across coil face
- 4 kJ/pulse

Lovberg and Dailey
1969, 1972, 1982, 1989, 1993, 1994